Modeling of the Current-Voltage Characteristics of CdTe Thin-Film and Bulk Heterojunction Organic Solar Cells

Salman Moazzem Arnab

A Thesis
in
the Department
of
Electrical and Computer Engineering

Presented in Partial Fulfillment of the Requirements
for the Degree of Master of Applied Science at
Concordia University
Montréal, Québec, Canada

August 2013

CONCORDIA UNIVERSITY
SCHOOL OF GRADUATE STUDIES

This is to certify that the thesis prepared

By: Salman Moazzem Arnab

Entitled: "Modeling of the Current-Voltage Characteristics of CdTe Thin-Film and Bulk Heterojunction Organic Solar Cells"

and submitted in partial fulfillment of the requirements for the degree of

Master of Applied Science (Electrical and Computer Engineering)

Complies with the regulations of this University and meets the accepted standards with respect to originality and quality.

Signed by the final examining committee:

_____ Chair
Dr. S. Williamson

_____ Examiner, External
Dr. A. Bhowmick (BCEE) To the Program

_____ Examiner
Dr. O. Tousignant

_____ Supervisor
Dr. M. Z. Kabir

Approved by: _____
Dr. W. E. Lynch, Chair
Department of Electrical and Computer Engineering

_____20_____

_____
Dr. C. W. Trueman
Interim Dean, Faculty of Engineering
and Computer Science

ABSTRACT

The popularity of solar cell has been on the rise over the past few years. In order to be the substitute the fossil fuels, the energy production cost from solar cells must be reduced further. A lot of effort has been made by the scientific community to produce cheap and green energy from solar cells. High absorption coefficient and cost effective deposition technique have made polycrystalline CdTe a suitable applicant for thin-film solar cell technology. On the other hand, bulk heterojunction polymer solar cells based on blends of conjugated polymers (P3HT) and fullerene derivatives (PCBM) have shown great potential to produce efficient organic solar cells.

Low availability of Te and need for enhancement of deposition speed influence to reduce the CdTe absorber layer. However, the overall cell efficiency of CdTe/CdS thin-film solar cell deteriorates unpredictably when the absorber width is reduced to sub-micron level. Deterioration of charge transport properties and their effects on voltage-dependent charge collection in submicron CdTe solar cells are believed to be responsible for this detrimental current-voltage. An analytical model for voltage-dependent photocurrent has been proposed in this thesis, considering partial depletion of the absorber and both electron and hole drift and diffusion in the depleted region and field free region, respectively, by solving continuity equations with proper boundary conditions. Exponential photon absorption and actual solar spectrum are considered to compute the photocurrent densities at entire output voltages. The results of the analytical model are verified by the 2D Taurus Medici device simulator. The model is also compared with

recently published experimental results on ultra-thin CdTe solar cells in order to determine the carrier transport properties (defects and carrier lifetimes) and effective doping concentrations.

The efficiency of bulk heterojunction organic solar cells is mostly controlled by the dissociation of bound electron and hole pairs (EHPs) and charge carrier transport properties after dissociation. An analytical model has been developed considering both drift and diffusion of charge carrier to examine the relative effects of EHP dissociation and charge collection on the current-voltage characteristics. The effects of annealing on carrier transport properties are also examined. The theoretical model is also verified by the published experimental data.

ACKNOWLEDGEMENTS

I am indebted to The Almighty for giving me the strength to complete my work.

I am grateful to all of my family members who have supported me through thick and thin over the past two years.

I would like to express my earnest gratitude to my research supervisor Dr. M. Zahangir Kabir for his encouragement, guidance, inspiration and financial support. Without his help and support, completing this work would not have been possible.

I am also grateful to my friends Mehran Khan and Arshi Islam, who have helped me on numerous occasions to complete this work.

Finally, I would like to thank Dr. Shaikh Asif Mahmood for his assistance as well as the other members of my research group, Khalid Sakib, Safayat-Al-Imam and Farzin Manouchehri.

TABLE OF CONTENTS

LIST OF FIGURES

LIST OF TABLES

LIST OF ABBREVIATIONS

IEA	-	International Energy Agency
PV	-	Photovoltaic
UN	-	United Nations
BHJ	-	Bulk heterojunction
EHP	-	Electron and hole pair
VB	-	Valance band
CB	-	Conduction band
AM	-	Air mass
2D	-	Two dimensional
HOMO	-	Highest occupied molecular orbital
LUMO	-	Lowest unoccupied molecular orbital
HOMO-A	-	HOMO of acceptor
HOMO-D	-	HOMO of donor
LUMO-A	-	LUMO of acceptor
LUMO-D	-	LUMO of donor
ASTM	-	American Society for Testing and Materials
ITO	-	Indium tin oxide
AgBr	-	Silver bromide
AgCl	-	Silver chloride
Pt	-	Platinum
Se	-	Selenium
Au	-	Gold
Si	-	Silicon

Ge	-	Germanium
B	-	Boron
P	-	Phosphorus
CdTe	-	Cadmium telluride
CdS	-	Cadmium sulfide
CIGS	-	Copper indium gallium selenide
a-Si:H	-	Hydrogenated amorphous Si
Te	-	Telluride
P3HT	-	Poly(3-hexylthiophene)
PCBM	-	[6,6]-phenyl C_{61}-butyric acid methylester
SnO_2	-	Tin dioxide
Cu	-	Copper
bis[70]PCBM	-	Bisadduct analogues of C_{70}
PEDOT:PSS	-	Poly(3,4-ethylenedioxythiophene) poly(styrenesulfonate)

LIST OF SYMBOLS

E_g	-	Bandgap
χ	-	Electron affinity
V_{oc}	-	Open circuit voltage
J_{sc}	-	Short circuit current density
FF	-	Fill factor
η	-	Overall cell efficiency
P_{max}	-	Maximum power point
R_s	-	Series resistance
R_{sh}	-	Shunt resistance
h	-	Planck's constant
c	-	Speed of light
λ	-	Wavelength of the incident photon
J_{ph}	-	Photocurrent density
J_d	-	Forward diode current density
n	-	Ideality factor
e	-	Elementary charge
k_b	-	Boltzmann's constant
T	-	Absolute temperature
J_o	-	Reverse saturation current density
L_1	-	Path length through the atmosphere
L_z	-	Zenith path length
θ	-	Solar zenith angle
F	-	Built-in electric field

S	-	Recombination velocity at the interface
N_a	-	Acceptor concentration
V_{bi}	-	Built-in potential
ε	-	Permittivity of the semiconductor
α	-	Absorption coefficient
L	-	Diffusion length
x_d	-	Length of the depletion region
W	-	Absorber width or the active layer width
V_o	-	Flat band voltage
V_t	-	Thermal velocity
τ	-	Carrier lifetime
μ	-	Carrier mobility
G	-	Photon generation rate
I_o	-	Intensity of the solar spectra
R	-	Loss factor
α_1	-	Absorption coefficient of the CdS window layer
d	-	Width of the CdS window layer
k_f	-	Geminate recombination rate
k_d	-	Separation rate of bound EHPs
a	-	Reaction radius
r_c	-	Onsager radius
S_1	-	Reactivity parameter
M	-	Escape probability
δp	-	Photo-generated hole concentration
δn	-	Photo-generated electron concentration

V_j	-	Junction voltage
δ	-	Penetration depth

CHAPTER 1

Introduction

Energy consumption rate is increasing day by day. In order to fulfill the uprising demand of energy for an advanced living standard, the modern human civilization depends mostly on fossil fuels [1]. From the chart in Fig. 1.1, displaying various sources of energy in the year 2011, it can be shown that 83% of the total consumed energy is produced from coal, natural gas and petroleum [2]. As these natural sources are non-renewable and limited, the world is quickly heading towards a serious energy crisis [3]. Another consequence of burning fossil fuels is global warming. The lowest predicted consumption of fossil fuel will cause the global temperature to increase by 1.1 to 2.9 degrees Celsius during the 21st century. However, in the worst possible prediction, the global temperature will rise by 2.4 to 6.4 degrees Celsius [4]. In order to prevent this crisis, scientists and researchers are trying with their best efforts to make renewable energy more popular and to utilize the unlimited solar energy efficiently. As the result of their hard work, the usage of solar energy has increased rapidly. The International Energy Agency (IEA) predicts that within the next 50 years, solar power generators will be efficient enough to fulfill most of the electricity demand of the world.

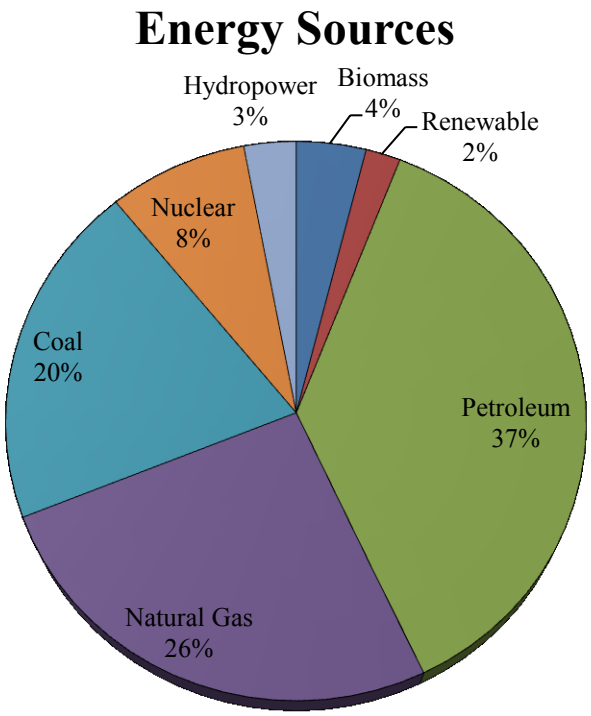

Figure 1.1 Energy consumption from various sources in 2011 [2]

1.1 Brief history of solar cells

Modern solar cells are the result of intense research work over the years. Evolutions of organic and inorganic photovoltaic (PV) cells over these years are described below.

1.1.1 Development of inorganic solar cells

In 1839, Alexandre Edmond Becquerel first noticed PV effect while he was working with silver bromide (AgBr) or silver chloride (AgCl) coated platinum (Pt) electrode in an electrolyte solution. He observed a small voltage change when sunlight struck upon the electrode. After 44 years, in 1883, Charles Fritts introduced the first solid state solar cell.

He created a junction by coating selenium (Se) with ultra-thin gold (Au) layer. The efficiency of his device was very low. Later in 1946, Russell Ohl introduced the modern semiconductor solar cell [5]. Daryl Chapin, Calvin Souther Fuller and Gerald Pearson fabricated the first practical solar cell at Bell Laboratories in 1954. The efficiency of their silicon (Si) based solar cell was 6%. Since 1954, there have been substantial improvements in solar cell technology.

1.1.2 Development of organic solar cells

Photoconductivity in an organic compound (anthracene) was first observed by Pochettino in 1906. In the early 1960s, PV effects were observed in organic materials after finding semiconducting properties in many common dyes (i.e. methylene blue) [6]. The efficiency of these cells was very low; namely, below 1%. In 1986, Ching W. Tang first introduced heterojunction organic solar cell by using copper phthalocyanine layer as light absorber and electronegative perylene carboxylic derivative. The efficiency of this organic solar cell was 1%. To improve the efficiency further, G. Yu introduced the concept of bulk heterojunction organic solar cell in 1995. Currently, an efficiency of 8% is achieved in literatures [7].

1.2 Different generations of solar cells

The solar cell technology has been divided into three main categories. Each of these categories is referred by the word ‘generation’. A brief discussion on different generations of solar cells is presented.

First generation solar cells are mainly made of pure silicon (Si) or germanium (Ge). In order to form a p-n junction, these materials are doped with boron (B) and phosphorus (P). These solar cells have higher efficiency compared to any other solar cells but in terms of price, these devices are costlier. The cost of first generation solar cells is comparatively high because a huge amount of pure materials are required to make these kinds of solar cells. The efficiency of first generation solar cells is quite close to the maximum theoretical efficiency. According to Shockley–Queisser limit, the maximum theoretical efficiency can be as high as 33.7% for a single p-n junction solar cell.

Second generation solar cells (commonly called thin-film) are cheap compared to first generation solar cells because these solar cells are made with less amount of pure materials. Even the material selection is done quite sensibly. Thin-film solar cells based on polycrystalline cadmium telluride (CdTe), polycrystalline copper indium gallium selenide (CIGS) and hydrogenated amorphous Si (a-Si:H) are the main three candidates of second generation solar cells. Other than these solar cells, organic solar cells also fall under this category. The availability of materials and cost effective fabrication process made second generation solar cells more popular.

Third generation solar cells are based on completely new concepts. Intensive research work is in progress to bring third generation solar cells into the market. The main goal of course is to achieve higher efficiency than the Shockley–Queisser limit. The technology used for third generation is somewhat ambiguous. Generally, it includes hot-carrier effects, multiple carrier ejection, photon upconversion and downconversion [8].

1.3 Growth of solar cell usage

Fossil fuels are the main sources of carbon emission and greenhouse gases and as mentioned before, the amount of fossil fuels is limited. In this context, energy from solar cells seems very attractive as it is clean, unlimited and environment friendly. However, fossil fuels still dominate the energy market in many countries because it requires comparatively less money to produce energy from fossil fuels than renewable energy sources.

Due to thorough research and mass production of solar cells, the price of energy (per watt) produced by solar cells has been decreasing drastically. As a result of this reduction in price, solar cells are becoming increasingly popular in the energy market. Figure 1.2 shows the worldwide solar cells growth from 2007 to 2011 [9]. This graph represents the total annual capacity (giga-watts) of installed solar cells. A growth rate of 172.22% is observed from 2009 to 2010, while an average growth rate (per year) from 2007 to 2011 was 80.47%.

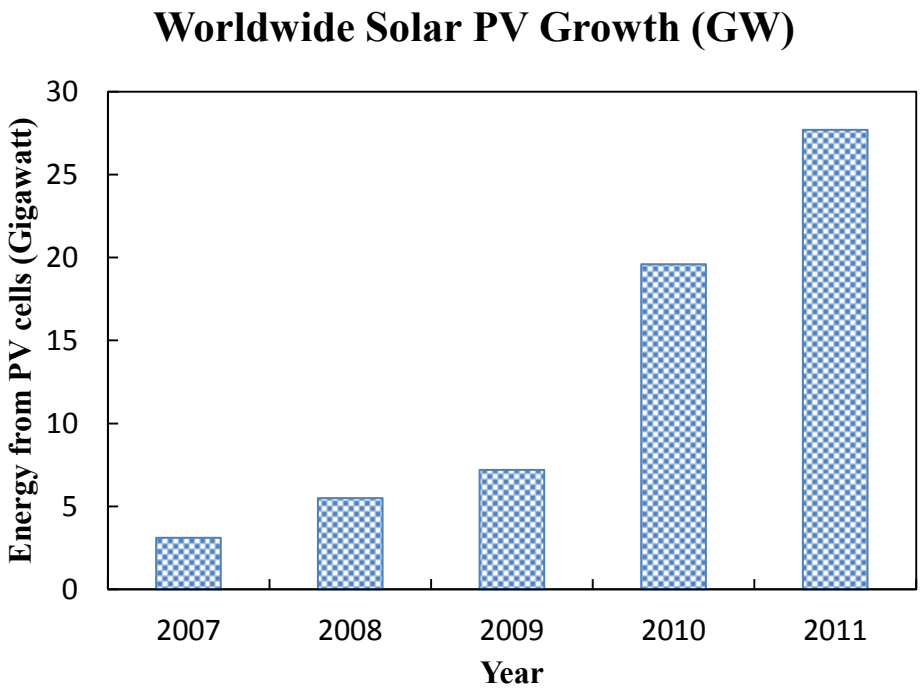

Figure 1.2 worldwide solar PVs growth from 2007 to 2011 [9]

On the other hand, organic solar cells are heading quickly towards achieving the minimum efficiency (10%) for commercialization [10]. It is predicted that organic solar cells will dominate the PV market in near future because of its attractive features, such as lower production cost and flexibility of organic molecules [11].

1.4 Solar cell market

PV prices have been reduced dramatically over last 30 years. It was $98 (U.S. dollar) per watt in 1975 but at the end of 2007, it reduced to about $4 per watt [12]. The average retail price decreased from $3.50 to $2.43 per watt over the course of 2011 [13]. For large-scale installations, price of solar energy goes down below $1 per watt. As time progresses, fossil fuels are getting more expensive. Meanwhile, solar cell technology is

getting cheaper. For instance, PV energy is now cheaper than the energy from nuclear power stations. Therefore, it is predicted that renewable energy technologies, such as solar cells will soon take over the current energy market. A crossover point when the cost of energy from solar power stations matches the cost of conventional electricity generation is usually referred to as grid parity. A projection of the prices of conventional energy and solar energy is shown in Figure 1.3 [14]. The estimated crossover points are highlighted.

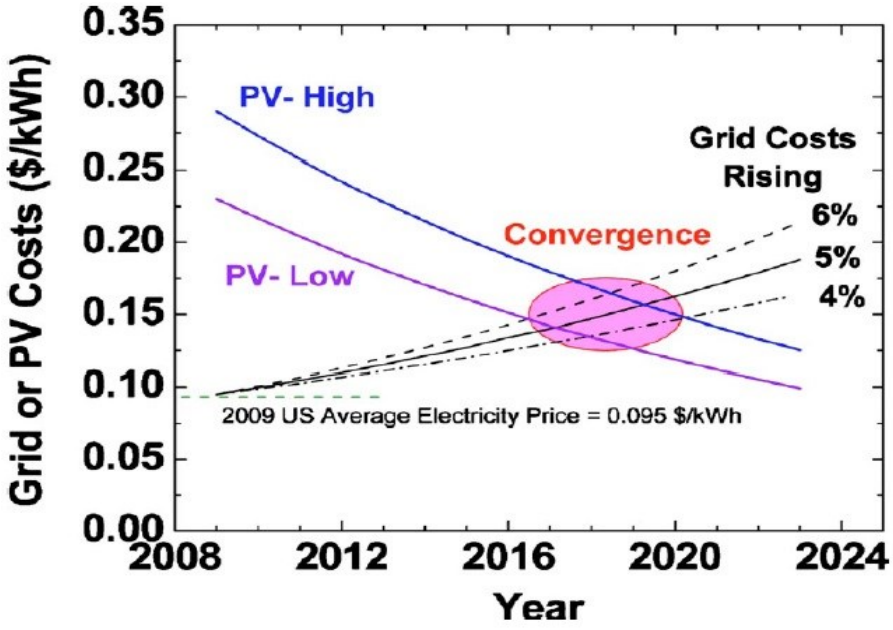

Figure 1.3 A projection of the prices of conventional energy source and solar energy and the estimated crossover point [14]

Due to insufficient efficiency and lack of proper industrial infrastructure, organic solar cells are not entirely commercialized yet. Also, organic solar cells' lifespan is not long

enough to fully penetrate the energy market. This technology requires further improvements to compete with the existing solar cells.

1.5 Application of solar cells

In many applications solar cells are the most viable option for power supply. For example, costly and heavy fuel-power sources for space vehicles (i.e. satellites and space telescopes), which require continuous power supply to recharge their batteries, can easily be substituted by light and comparatively cheap solar panels. Therefore, solar cell is the best option for supplying electrical power to satellites [15].

Grid electricity or fossil fuel is inaccessible to over 2 million villages in the world according to UN estimation. Local PV power stations for the rural parts of the world can change the whole scenario. In many places PV power stations are already functional for supplying power into the electricity grid. People are showing more interest in solar panels to obtain their electricity from clean, non-polluting, renewable source. Solar energy is not restricted within residential uses only. It is also a very popular source of energy for commercial uses. For many years, solar energy has been the best choice for the industries that are located in the rural areas.

Solar cells are also used in automobile industry. The cars powered solely by solar energy are slow and incapable of carrying heavy weight as the amount of power generated by solar panels mounted on the cars is insufficient. On the other hand, hybrid cars distribute the power consumption between solar power and fossil fuel. Since the introduction of the

first solar powered car by Ed Passerini, intensive research has been carried out by the automobile industry to introduce a vehicle that would run solely on solar energy.

1.6 Research motivation

1.6.1 CdS/CdTe solar cells

Thin film solar cells have become very popular in inorganic solar cell industry due to drop in production cost together with reasonably higher power efficiency [14,16]. Efficient absorption of solar spectrum within about a micron-thick absorption layer, easy and cost effective deposition techniques and excellent charge collection property have made polycrystalline CdTe a strong candidate for thin film solar cell technology [14,17]. Low availability of Te and need for enhancement of deposition speed made submicron CdTe absorber layer a popular research topic in thin film photovoltaic (PV) technology [17]. However, when the thickness of the absorber layer (W) is reduced to submicron level, the open circuit voltage (V_{oc}) and fill factor (FF) of CdTe solar cells deteriorates unpredictably [18]. Deterioration of charge transport properties and their effects on voltage-dependent charge collection in submicron CdTe solar cells are believed to be responsible for this detrimental current-voltage (J-V) characteristic [17]. Increased recombination states in the absorber layer, series resistance, and leakage current are considered as the reasons for reduction of V_{oc} and FF in ultra-thin CdTe solar cells [17,19].

Few analytical [20] and numerical [19] models have been proposed in the literature for calculating voltage-dependent photocurrent in thin film solar cells. Hegedus *et al.* [20] have mentioned few models for voltage dependent collection efficiency. The short circuit current density (J_{sc}) is calculated considering complete charge collection. The most successful model computes photocurrent by considering that photo-generation occurs only at the CdS-CdTe interface. On the other hand, Anjan and Kabir [21] have derived an analytical model for external voltage-dependent photocurrent. While all the previous models assumed the full depletion of the absorber layer for the entire voltage range, in reality, the absorber layer is partially depleted at operating (relatively high) output voltage. Therefore, a more realistic analytical/numerical model is required to properly describe the current-voltage characteristics.

1.6.2 P3HT:PCBM bulk heterojunction polymer solar cells

Bulk heterojunction (BHJ) polymer solar cells based on blends of conjugated polymers and fullerene derivatives have already been established as the next generation solar cell for their high conversion efficiency, easy fabrication and abundant availability [22]. Poly(3-hexylthiophene) (P3HT) and [6,6]-phenyl C_{61}-butyric acid methylester (PCBM) are the most promising candidates among polymer and fullerene derivatives, respectively of BHJ solar cells. Due to high hole mobility, PCBM is one of the best options for using it as a fullerene derivative [23]. However, the high binding energy of the bound electron-hole pairs (EHPs) in the blend reduces the photo-generation in BHJ polymer solar cells [24]. Therefore the photocurrent largely depends on the dissociation efficiency of bound EHPs. The charge carrier transport properties also have great influence on the overall cell

efficiency of organic solar cells [25]. Therefore, a physics-based model relating the quantitative effects of charge transport properties and dissociation of bound EHPs of organic materials on the *J-V* characteristic is inevitable.

Few models exist in the literature for calculating voltage-dependent photocurrent in BHJ polymer solar cells [25,26.27]. The first model is based on an empirical expression and uses Braun model (which is based on Onsager theory) to compute the dissociation efficiency. However, there is a significant difference between Braun model and the exact extension of Onsager theory. The empirical expression fails to explain the exact physics of the charge transport mechanism in organic materials. The latter model does not consider direct recombination of photo-carriers and also fails to explain the dissociation of bound EHPs.

1.7 Research objective

The main objective of this research is to improve the understanding of device operation in organic and inorganic solar cells by physics-based analytical/numerical modeling. Separate research objective for organic and inorganic solar cells are presented in the following subsections.

1.7.1 Thin-film solar cell

The photo-generated charge carriers move by drift and diffusion mechanisms in the depletion and outside of the depletion regions, respectively, because of negligible built-in

electric field that is found at the outside of the depleted region. The objectives of this research work are defined considering the facts that are mentioned above. A brief outline of the objectives is the following:

(a) To develop an analytical model for voltage-dependent photocurrent, considering both electron and hole drift in the depleted region and diffusion in the field free region by solving continuity equations. The model considers exponential photon absorption and actual solar spectrum. The overall load current considers the effect of voltage-dependent forward dark current consisting recombination current in the depleted region and the diffusion current in the field-free region.

(b) To verify the results of the analytical model by the 2D Taurus Medici device simulator and recently published experimental results on ultra-thin CdTe solar cells.

(c) To determine the effects of carrier transport properties and effective doping concentrations on ultra-thin CdTe solar cells.

1.7.2 Organic solar cell

The absence of exact modeling of device behavior is one of the main obstacles in developing organic solar cell technology [28]. Modeling device behavior plays an important role to realize the physics of a device. As mentioned above, dissociation efficiency has a great influence on the total cell performance. Thus accuracy in computing dissociation efficiency is necessary to predict the exact output. The *J-V* characteristics also depend on charge transportation mechanism. By taking these facts into account, the research objectives for organic solar cells are,

(a) To develop an analytical model for voltage-dependent photocurrent considering drift and diffusion of the charge carriers in P3HT:PCBM organic solar cell. The model incorporates electric field dependent escape probability that agrees well with the exact extension of Onsager theory.

(b) To compare the analytical model with the published experimental results in order to validate the model and to determine the carrier transport properties (defects, carrier mobility and lifetime) and effects of charge dissociation.

1.8 Thesis outline

This thesis contains six chapters. Following this introductory chapter, the second chapter contains few basic theories and a brief discussion on the existing models for *J-V* characteristics of CdS/CdTe thin-film and P3HT:PCBM BHJ solar cells. In the third chapter, the numerical model has been discussed in details. The developed analytical model for CdS/CdTe is explained in the fourth chapter. This chapter also contains the simulation results of the model and some brief discussions. The fifth chapter contains the analytical *J-V* model of P3HT:PCBM blend. The effects of various parameters and dissociation efficiency are illustrated in the results and discussion part of this chapter. Conclusion, contribution and future work is presented in the last chapter.

CHAPTER 2

Background Theory

2.1 Physical structure of solar cells

The structures of solar cells mainly depend on the properties of the material of the solar cells. Therefore, bulk polymer and thin-film solar cells have different physical structures. A brief discussion on these different structures is given in the following sections.

2.1.1 Structure of CdS/CdTe thin-film solar cell

In CdS/CdTe thin film solar cells, CdS and CdTe layers are known as the window layer and the absorber layer, respectively. The physical structure of a CdS/CdTe is shown in Fig. 2.1. CdTe acts as the absorber layer because the incident photons are absorbed in this layer as the bandgap (E_g) of CdTe is as low as ~1.45 eV. The width of this layer can vary from 0.5-3.5 μm. Sufficiently long CdTe layer can absorb photons up to ~900 nm of the solar spectrum. As the absorber layer is lightly doped and the window layer is highly doped, as shown in Fig. 2.1, the depletion layer tends to extend through the CdTe layer. Negligible amount of photon is absorbed in CdS due to its large E_g (~2.42 eV) and very thin width (~0.06-0.2 μm). The oxide layer (SnO_2 in Fig. 2.1) between CdS and glass layer is used to match the refractive indices for higher light absorption and to reduce

series resistance. The back electrode is copper (Cu) coated gold (Au), which can reduce the hole barrier at the back contact.

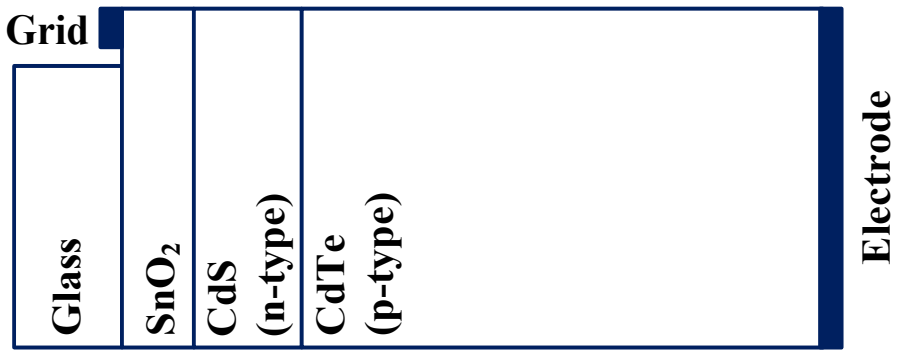

Figure 2.1 Schematic diagram of a CdS/CdTe thin film solar cell

2.1.2 Structure of P3HT:PCBM blend organic solar cell

The typical device configuration of a BHJ polymer solar cell is shown in Fig. 2.2, where P3HT and PCBM are used as donor and acceptor materials, respectively. In order to increase the dissociation efficiency, P3HT and PCBM are blended together to form the active layer. The weight ratio of P3HT:PCBM is varied to control few properties (i.e., absorption coefficient) for better efficiency. The length of the active layer (W) can vary from 100 to 250nm. Poly(3,4-ethylenedioxythiophene) poly(styrenesulfonate) or PEDOT:PSS is the transparent conductive polymer layer between the active layer and the anode. This layer acts as a buffer layer which facilitates the photo generated holes to travel to the front contact. Indium Tin Oxide (ITO) forms an ohmic contact for easy transport of the generated carriers and also avoids unwanted absorption of the solar spectra.

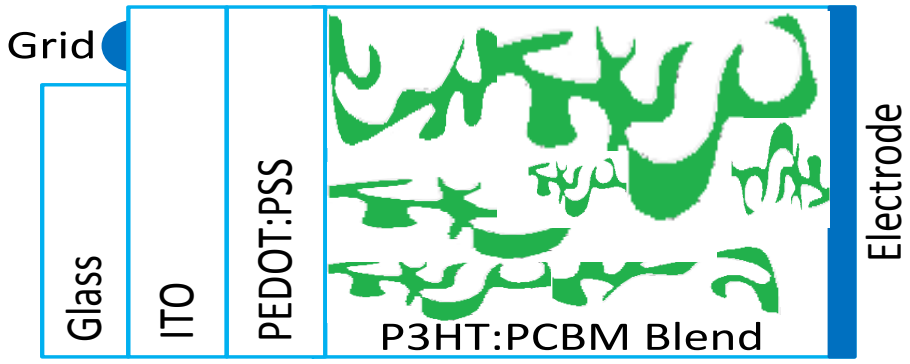

Figure 2.2 Schematic diagram of a P3HT:PCBM BHJ solar cell

2.2 Material properties

The properties of the materials have significant effects on cell performance. As mentioned earlier, light is absorbed in the active layer of bulk organic solar cells and in the absorber layer of inorganic thin-film solar cells. Therefore, material properties of CdTe and P3HT:PCBM blend play a vital role in photo-current production.

2.2.1 Polycrystalline cadmium telluride

The polycrystalline materials consist of many single-crystal regions unlike crystalline materials which have regular geometric periodicity throughout the entire volume [29]. In polycrystalline materials, the single-crystal regions are known as grains and the grains are separated by grain boundaries. In most of the polycrystalline materials, impurities are accumulated at the grain boundaries. Thus the grain boundaries tend to degrade the electrical and physical properties of the polycrystalline materials. Figure 2.3 shows the crystal structure of a polycrystalline material. The grain boundaries of polycrystalline

CdTe are not highly electrically active. Thus CdTe is well suited for photo-generated charge carrier transportation [30].

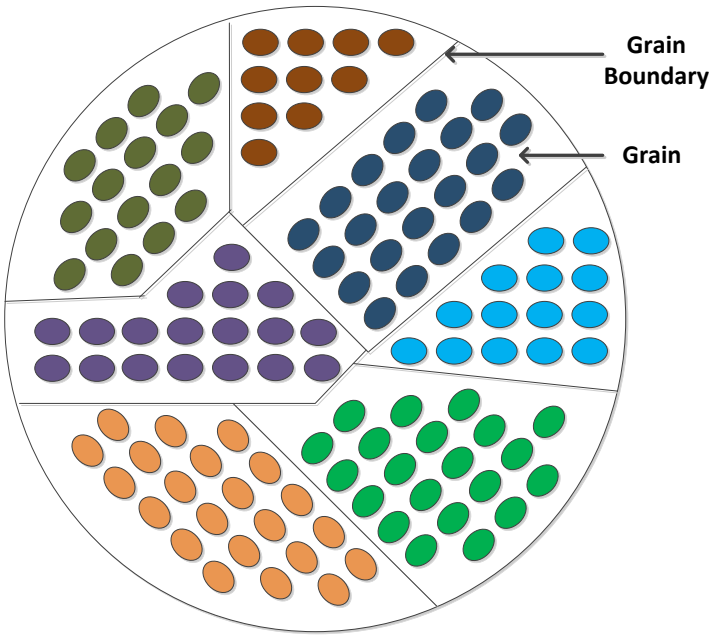

Figure 2.3 Schematic of polycrystalline material

In 1947, Frerichs synthesized CdTe for the first time by combining Cd and Te vapors with each other in a hydrogen atmosphere [31]. CdTe is a compound semiconductor with a direct optical band gap of 1.45 eV. This made CdTe an excellent absorber of solar spectrum and thus a suitable material for photovoltaic energy conversion. Due to high absorption coefficient of CdTe, high quantum efficiency has been noticed in CdTe thin-film solar cells. Figure 2.4 shows the absorption coefficient of CdTe as a function of wavelength.

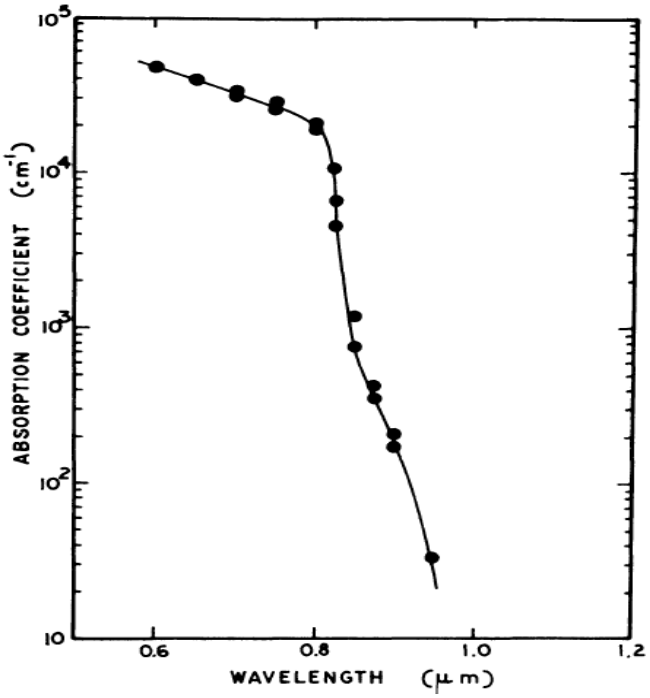

Figure 2.4 Absorption coefficient of CdTe as the function of wavelength [32]

High absorption coefficient of CdTe also allows the absorber layer to absorb most of the absorbable photons within only 2 μm of thickness (see Section 3.6.1). The photon absorption reduces by only 4% when the absorber width decreases from 5 to 0.5 μm [33]. Whereas, the absorber made of crystalline silicon requires 200 μm of width to absorb 92% of the useful sunlight [30].

2.2.2 Poly(3-hexylthiophene) and [6,6]-phenyl C_{61}-butyric acid methylester blend

In recent years, conjugated polymers have drawn much attention due to its solubility and electrical conductivity. Flexibility is also another promising feature of polymers. Among all polymers, P3HT is widely used in organic solar cell technology due to its relatively higher carrier mobility and higher absorption coefficient (in order of 10^5 cm^{-1}) [34]. The

bandgap of P3HT is around ~1.7 eV which is much lower than the bandgap of PCBM (~2.3 eV). Thus incident photons are mainly absorbed in the donor material. The chemical structures of P3HT and PCBM are given in Fig. 1 of Ref. [35].

The PCBM (electron acceptor) is a fullerene derivative of the C_{60}. The electron affinity (χ) of this fullerene is ~3.7 eV which is comparatively higher than that of P3HT. Therefore, photo-generated electrons in the lowest unoccupied molecular orbital (LUMO) of the donor (LUMO-D) are easily transferred to the LUMO of the acceptor (LUMO-A). The high solubility in organic solvent of PCBM makes it well suited for the BHJ solar cell. This feature of PCBM allows preparing fine homogeneous BHJs and printable solar cells. The fine tuning of the band gap of PCBM reduces the offset between the LUMO-D and the LUMO-A which in turn increases the V_{oc} [36]. The band gap of PCBM can be modified by several ways, i.e. synthesizing bisadduct analogue of PCBM [36] and placing substituents on the phenyl ring or altering chemical structure of organic material by electron irradiation [37].

Annealing at various temperatures and increasing the weight ratio of P3HT in the blend improve the absorption coefficient of the active layer [35,38]. Figure 2.5 shows the absorption coefficient of the blend for various weight ratios between P3HT and PCBM [35]. As the ratio of PCBM in the blend decreases, the absorption coefficient below 425 nm decreases whereas that between 425 and 700 nm grows gradually. A sharp decrease and distortion of the shape of the absorption coefficient are observed when the PCBM content in the blend increases beyond the 1:1 composition. This verifies the increment of

the volume occupied by PCBM in the blend (refer to the absorption coefficient of P3HT and PCBM in ref. [39]). In conclusion, the intermolecular packing structure of P3HT can be preserved if the weight ratio of PCBM is restricted below 1:1 composition [35].

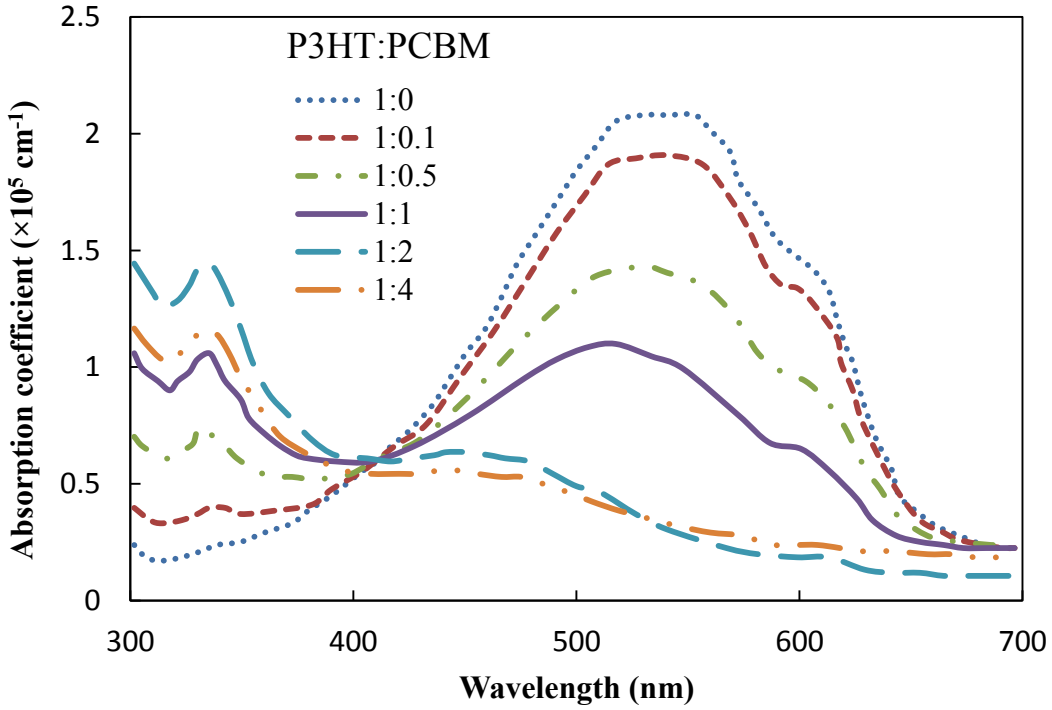

Figure 2.5 Absorption coefficients of the active layer for different weight ratio between P3HT and PCBM [35]

Figure 2.6 shows the effect of annealing on the absorption coefficient (from ref. [38]) of the blend. The annealing temperature has been varied from 100° to 125°C. The thermal diffusion of PCBM molecules into large PCBM aggregates increases when the temperature increases [38]. As a consequence, P3HT can aggregate in the PCBM free regions and form crystalline P3HT. Thus the annealing process increases the crystallinity of P3HT; which, in turn increases the absorption coefficient of the blend.

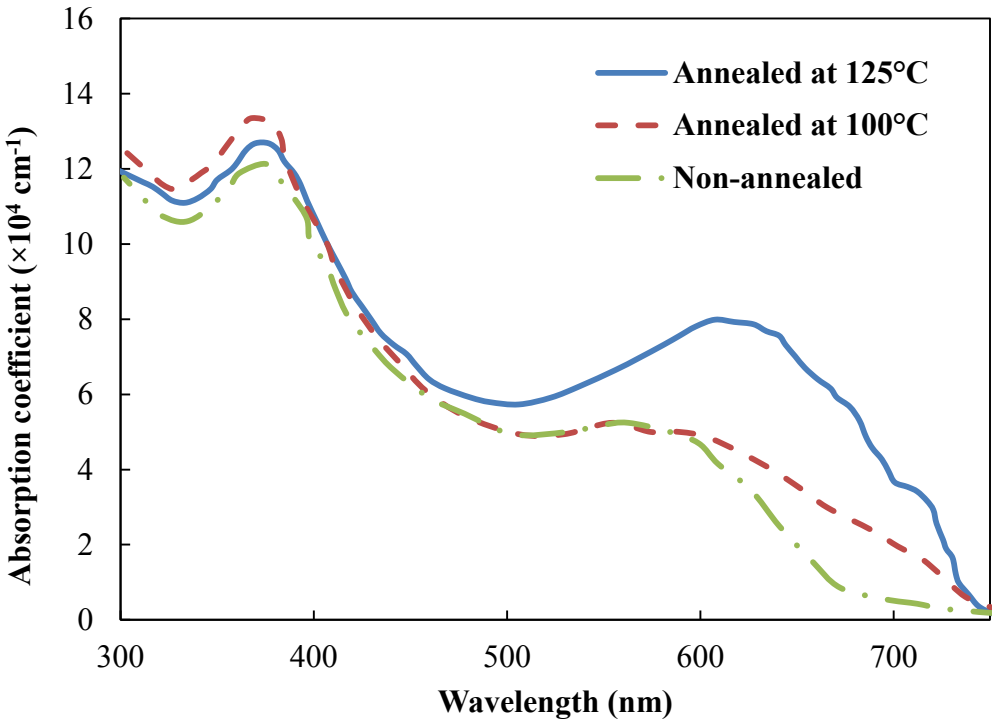

Figure 2.6 Effects of different annealing temperatures on absorption coefficient of P3HT:PCBM blend [38]

2.3 Photovoltaic energy conversion

Solar cells convert solar energy to electrical energy in the form of current and voltage. This conversion is done in basic three steps. These steps are given below.

(a) Photon absorption and creation of bound electron hole pairs: Photons are mostly absorbed at the absorber and donor layers of CdS/CdTe and P3HT:PCBM solar cells, respectively. Electrons jump from valance band (VB) to conduction band (CB) in inorganic solar cells or from highest occupied molecular orbital (HOMO) to LUMO in organic solar cells creating holes in the VB and in the HOMO, respectively. Thus the

incident photons require enough energy (E) to make this transition. The energy of a photon is [29]

$$E = \frac{hc}{\lambda} \tag{2.1}$$

Here, h is the Planck's constant, c is the speed of light and λ is the wavelength of the photon. The energy E has to be more than or equal to E_g of the absorber for successful absorption of the incident photons. Figure 2.7 (step- i) shows the photon absorption process in CdS/CdTe and P3HT:PCBM solar cells. As a result of photons absorption, bound electron hole pairs (EHPs) are formed.

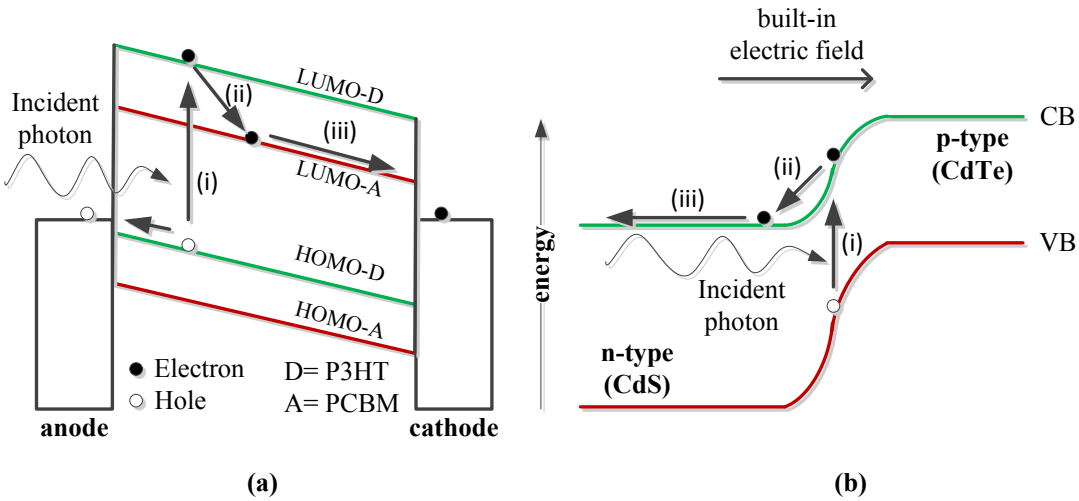

Figure 2.7 The process of photon absorption to photocurrent generation in (a) P3HT:PCBM blend and (b) CdS/CdTe thin-film solar cell

(b) Creation of free charge carriers: The built-in electric field between acceptor and donor assists the bound EHPs separation process, which is known as dissociation of bound EHPs. The dissociation rate depends on the binding energy of the bound EHPs. The binding energy is the coulombic attraction between an electron and a hole. This

binding energy is very high in organic materials due to their low dielectric constant. Therefore, the required energy for the bound EHPs to become free carriers in P3HT:PCBM solar cells is higher compared to that in CdS/CdTe solar cells. The built-in electric field provides this extra energy to the bound EHPs. Therefore, it is necessary for the bound EHPs to travel near to the acceptor and donor interface for dissociation (in BHJ solar cell). Figure 2.7 (step- ii) shows the dissociation of EHPs.

(c) Charge collection: These free charge carriers travel towards the respective electrodes and flow through an external circuit. In P3HT:PCBM solar cells, free electrons jump from the LUMO-D to the LUMO-A and travel through the acceptor material (PCBM) towards the cathode. The holes remain in the donor material (P3HT) and travel towards the anode. Collection of the charge carriers at the electrodes depends on their work functions. Figure 2.7 (step- iii) shows the movement of photo generated holes and electrons in a P3HT:PCBM blend.

In case of CdS/CdTe thin-film solar cells, free holes travel in the direction of the built-in electric field while the free electrons travel in the opposite direction. Thus the photo generated holes remain in CdTe layer and travel towards the back contact by both drift and diffusion mechanism. Whereas the photo generated electrons travel towards the window layer. Figure 2.7 (step- iii) shows the movement of photo generated holes and electrons in a CdS/CdTe thin-film solar cell. The back contact can block the holes to flow through the external circuit. In order to reduce back contact effects, the back electrode in

coated with Cu, and the metal used for back contact is selected according to its work function.

2.4 Characterization

The output current density of solar cells as function of the output voltage is known as *J-V* characterization. *J-V* curve provides most of the necessary information to characterize both organic and inorganic solar cells. For example, open circuit voltage (V_{oc}), short circuit current density (J_{sc}) , fill factor (*FF*), overall cell efficiency (η), maximum power point (P_{max}), series resistance (R_s), and shunt resistance (R_p) can be evaluated from the *J-V* curve.

A parallel connection between a current source and a rectifying diode represents an ideal solar cell. It is known as "one-diode model". Figure 2.8a shows an equivalent circuit model for an ideal solar cell. A more practical model can be represented by adding one series resistor and one parallel resistor with the equivalent circuit model of an ideal solar cell. Figure 2.8b shows the practical equivalent circuit model. Thus the *J-V* curve can be explained by the Shockley solar cell equation,

$$J(V) = J_d(V) + \frac{V - JR_s}{R_p} - J_{ph}(V) \qquad (2.2)$$

where V is the output voltage, J_{ph} is the photocurrent density, R_s is the series resistance, R_p is the shunt resistance and J_d is the forward diode current density.

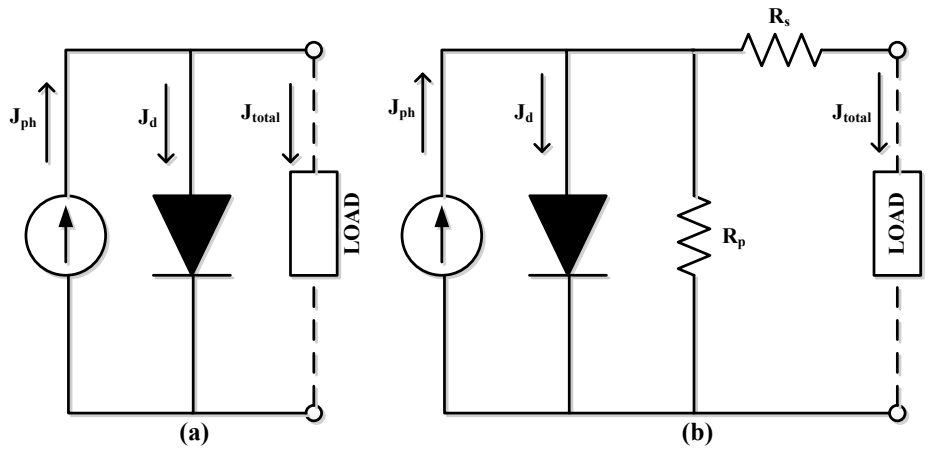

Figure 2.8 Equivalent circuit models of (a) ideal and (b) practical solar cells

2.4.1 Open circuit voltage

The V_{oc} is the voltage across the output terminal when the circuit is not connected with a load which implies that the output terminal is open (infinite resistance). Figure 2.9 shows the V_{oc} in a *J-V* curve. In ideal case, the V_{oc} can be calculated by the following equation.

$$V_{oc} = n\left(\frac{k_b T}{e}\right) ln\left(1 + \frac{J_{ph}}{J_o}\right) \tag{2.3}$$

In the equation above, n is the ideality factor, e is the elementary charge, k_b is the Boltzmann's constant, T is the absolute temperature, and J_o is the reverse saturation current density.

2.4.2 Short circuit current density

The short circuit current density is the current density flowing through the circuit while the output terminal is in short circuit condition which implies that the voltage across the

output terminal is zero. In ideal case, the short circuit current density is equal to the photocurrent. Figure 2.9 shows the J_{sc} in a *J-V* curve.

2.4.3 Fill factor

Solar cell performance can also be evaluated by calculating the fill factor from the *J-V* curve of a solar cell. Fill factor is the ratio of maximum power to maximum theoretical power. The maximum theoretical power can be calculated by multiplying the short circuit current density to the open circuit voltage. The expression for fill factor is given by,

$$FF = \frac{J_{max}V_{max}}{J_{sc}V_{oc}} \tag{2.4}$$

where, J_{max} and V_{max} is the current density and voltage, respectively, for maximum output power (P_{max}) . Figure 2.9 shows J_{max}, V_{max} and, P_{max} point (where solar cells usually operate).

2.4.4 Overall cell efficiency

Overall cell efficiency is the ratio of maximum output power to the input power. The input power is the rate at which solar energy reaches a unit area on the solar cell illuminated surface. It is known as solar irradiance and the unit is W/m^2. The overall cell efficiency is given by the following expression,

$$\eta = \frac{P_{max}}{P_{in}} = \frac{FF \times V_{oc}J_{sc}}{P_{in}} \tag{2.5}$$

The relative length of the optical path through the atmosphere around the world is calculated by air mass coefficient. The relative optical path is the ratio of the path length through the atmosphere (L_1) to the zenith path length (L_z).

$$AM = \frac{L_1}{L_z} \approx sec\theta \tag{2.6}$$

Here, θ is the angle (solar zenith angle) between L_1 and L_z. AM 1.5 corresponds to a θ of 48.2°. Figure 2.10 illustrates the AM 1.5 condition.

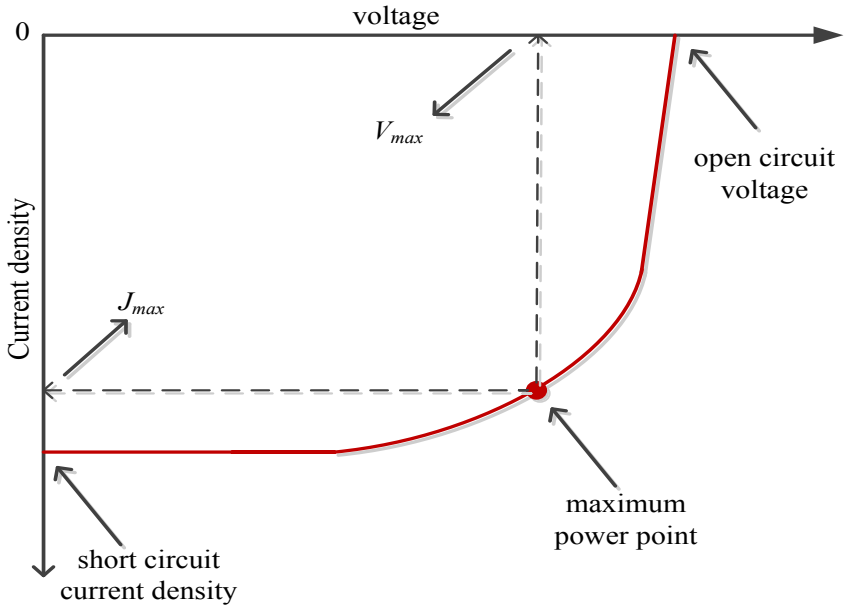

Figure 2.9 A typical *J-V* curve indicating open circuit voltage, short circuit current density, maximum power point, J_{max}, and V_{max}

2.4.5 Series resistance

The series resistance in a solar cell results from the movement of the charge carriers through the semiconductor materials, contact resistance (resistance between semiconductor and electrode) and the resistance of the electrode materials. Series

resistance mainly reduces the fill factor of solar cell. However, large value of series resistance can also decrease the J_{sc}. As mentioned above, series resistance can be calculated from the *J-V* curve of a solar cell. The slope of the *J-V* curve at the V_{oc} point is the series resistance of a cell. The effect of series resistance is illustrated in Fig. 4.7 (in chapter 4).

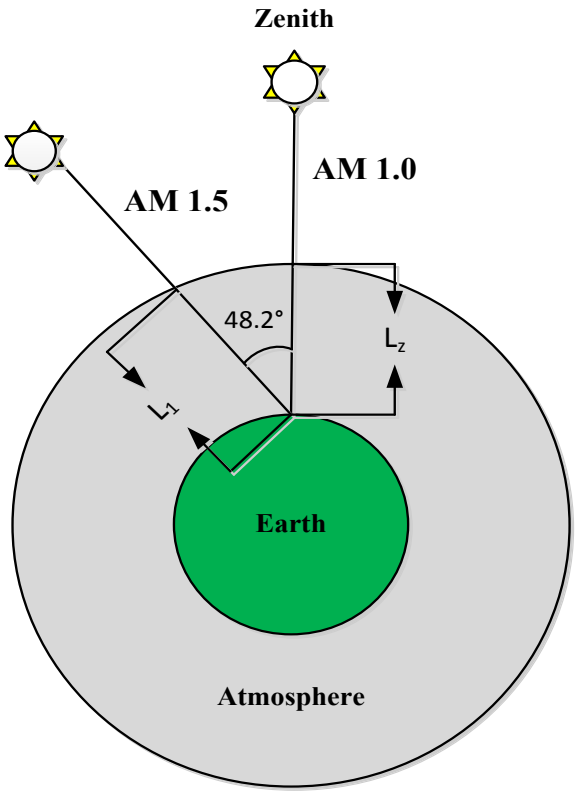

Figure 2.10 Illustration of the effect of incident angle on the light path through the atmosphere

2.4.6 Parallel resistance

Manufacturing defects can create shunt path for the photo generated carriers. Instead of travelling through the external circuit, the photo generated carriers can bypass through the shunt paths. Low parallel resistance reduces photo-current flow through the external

circuit and encourages the carriers to flow through the shunt path. The effect of parallel resistance is severe at low voltages.

2.5 Existing *J-V* characteristics models

The modeling of characteristics provides better insight of devices and also explains the device operation [19]. Device modeling can assist us to improve the design of a specific device and also helps to compare various structures. The values of material parameters can be optimized with the help of such models. Many *J-V* characteristic models for both organic and inorganic solar cells exist in the literature. A brief discussion on few important models is given in the following sections.

2.5.1 Models for *J-V* characteristics of CdS/CdTe thin-film solar cells

Hegedus *et al.* [20] mentioned in their work that the principle of superposition is not applicable for polycrystalline solar cells. Figure 2.11 proves the fact for an a-Si solar cell. The principle of superposition requires the dark current to shift down by a constant value of photocurrent (J_{sc}, if 100% collection efficiency is assumed). Superposition may occur in crystalline solar cells because crystalline semiconductors have negligible series resistance. As shown in Fig. 2.11, there is a substantial amount of loss between light current and shifted curve (estimated by applying the principle of superposition). Therefore, the total current density is not the difference between dark current and constant photo current only. It indicates that the photo-generated charge collection efficiency is not constant for all voltages; rather, it is a function of the output voltage.

They also explained three voltage dependent collection efficiency models for thin-film solar cells. These models are based on the concept that the maximum photocurrent is constant and multiplied by voltage dependent collection efficiency as shown in the equation below [40,41,42]

$$J_{ph}(V) = J'_{ph} \times \eta_c(V) \tag{2.7}$$

here, J_{ph} is the total photocurrent density, J'_{ph} is the maximum photocurrent density for complete collection of photo carriers, η_c is the voltage dependent collection efficiency and V is the applied voltage. The total current density can be expressed by

$$J(V) = J_d(V) + \frac{V - JR_s}{R_p} - J_{ph}(V) \tag{2.8}$$

here, J_d is the forward diode or dark current density, R_s is the series resistance, and R_p is the shunt resistance. Eq. (2.7) shows that the superposition principle can occur if η_c=1 for all values of output voltages.

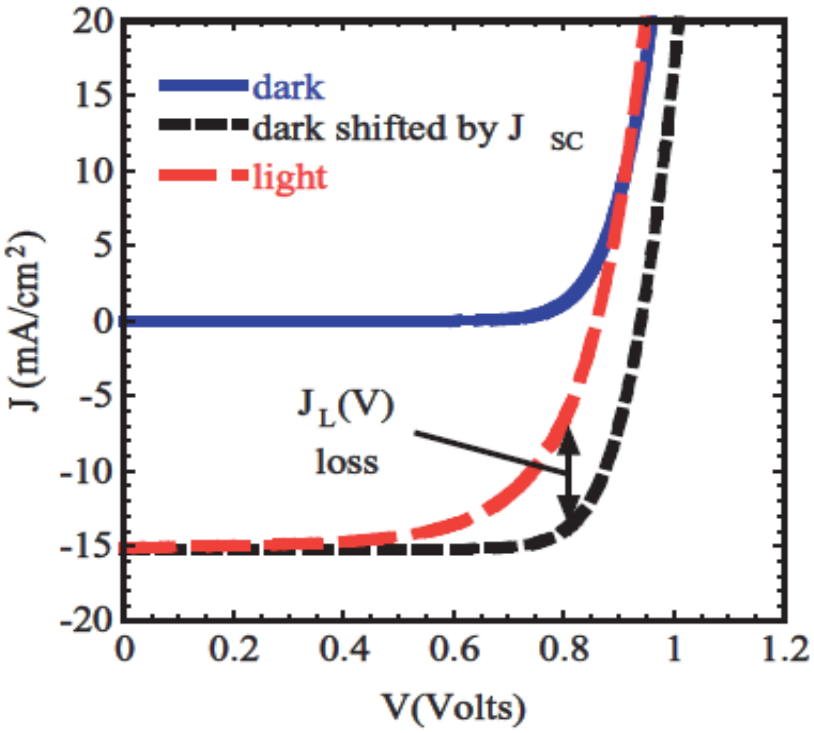

Figure 2.11 Dark current, light current and shifted current of an a-Si solar cell [20]

The first model considers interface recombination and drift-collection loss and presents the voltage dependent collection efficiency by the following empirical equation

$$\eta_c(V) = \frac{\mu F(V)}{S+\mu F(V)} \tag{2.9}$$

where, μ is the carrier mobility, F is the built-in electric field, S is the recombination velocity at the interface. The built-in electric field can be expressed as

$$F(V) = \sqrt{\frac{2eN_a(V_{bi}-V)}{\varepsilon}} \tag{2.10}$$

where, e is the elementary charge, N_a is the acceptor concentration, V_{bi} is the built-in potential and ε is the permittivity of the semiconductor.

The second model considers voltage dependent depletion layer width and a fixed diffusion length of the carriers to calculate the collection efficiency. The empirical equation of η_c,

$$\eta_c(V) = 1 - \frac{e^{-\alpha x_d(V)}}{1+\alpha L} \tag{2.11}$$

where, α is the absorption coefficient, L is the diffusion length and x_d is the length of the depletion region or

$$x_d(V) = \sqrt{\frac{2\varepsilon(V_{bi}-V)}{eN_a}} \tag{2.12}$$

This model assumes that the carriers, which are generated outside of the depletion region and cannot diffuse back to the depletion region after generation, are lost. These photo-generated carriers do not contribute to the photo current density.

The third and the most successful model, is based on recombination in the depletion region. According to this model, the charge collection is

$$\eta_c(V) = X(V)\left\{1 - e^{(-X(V)^{-1})}\right\} \tag{2.13}$$

where

$$X(V) = X_C\left(1 - \frac{V}{V_o}\right) \tag{2.14}$$

where, $Xc = \frac{\mu\tau V_{bi}}{W^2}$, W is the absorber width, V_o is the flat band voltage and τ is the carrier lifetime. The model assumes full depletion of absorber layer and all incident photons are absorbed at the interface of CdS/CdTe layer.

These models calculate the short circuit current density, considering complete charge collection. The most successful model (Eq. 2.13) calculates photocurrent by considering that all incident photons generate EHPs at the CdS-CdTe interface of the absorber layer, whereas the photons are absorbed exponentially across the absorber layer [21]. Another unrealistic assumption in that model is that the carrier injection from the neutral region has been assumed to be negligible. Furthermore, the mentioned models use many fitting parameters, such as reverse saturation current, effective attenuation coefficient, series resistance, and carrier ranges.

Recently, Anjan and Kabir [21] have derived an analytical model for external voltage-dependent photocurrent by solving the continuity equations for both holes and electrons. The photocurrent density due to holes is given below

$$J_p(\lambda, V) = \frac{eGW}{(\tau_p^{-1} - \Delta^{-1})}\left[\Delta\left(1 - e^{-\frac{1}{\Delta}}\right) - \tau_p\left(1 - e^{-\frac{1}{\tau_p}}\right)\right] \quad (2.15)$$

with $\tau_p = \frac{\mu_p \tau_p' F}{W}$ and $\Delta = \frac{1}{\alpha W}$

where, G is the photon generation rate, W is the width of the absorber layer and τ_p' is the hole lifetime. The subscript p represents holes. The following expression presents the photocurrent density due to electrons

$$J_n(\lambda, V) = \frac{eGW}{(\tau_n^{-1}+\Delta^{-1})}\left[\Delta\left(1 - e^{-\frac{1}{\Delta}}\right) - \tau_n\left(e^{-\frac{1}{\Delta}} - e^{-\frac{1}{\Delta}-\frac{1}{\tau_n}}\right)\right] \quad (2.16)$$

where, $\tau_n = \frac{\mu_n \tau_n' F}{W}$ and the subscript *n* stands for electrons in the absorber layer. The total current is calculated by considering voltage dependent dark current density.

The photo carriers, which are generated in the neutral region, have certain impacts on the *J-V* characteristics of a thin-film solar cell. However, the previous model, assumed the full depletion of the absorber layer for the entire voltage range. Hence, the effects of the neutral region photo carriers to the cell performance were totally neglected.

2.5.2 Models for *J-V* characteristics of P3HT:PCBM blends

In an ideal organic solar cell, the photo current density, is independent of output voltage and can be given by [25]

$$J_{ph} = eGW \quad (2.17)$$

where, *W* is the width of the active layer. Since the recombination of the charge carriers is negligible in ideal solar cells, the photo current can be determined directly from the generation (as shown in eq. 2.17). In such solar cells, the carriers can successfully leave the device without being recombined, which means the carrier lifetime is longer than the transit time (time required to travel through the active layer).

However, Sokel and Hughes [26] have pointed out that the previous equation cannot predict the photocurrent at the operating output voltage as the diffusion of charge carriers is totally neglected. They proposed a model for voltage dependent photocurrent which includes the diffusion component in the total photo current density

$$J_{ph}(V) = eGW\left[\frac{e^{\frac{V}{V_t}}+1}{e^{\frac{V}{V_t}}-1} - \frac{2V_t}{V}\right] \tag{2.18}$$

here, V_t is the thermal voltage. However, their proposed model is based on an empirical expression. It is hard to find the exact effects of various important parameters on *J-V* curve with this model.

As mentioned earlier, all bound EHPs cannot produce free electrons and holes. Thus the performance of BHJ solar cells greatly depends on dissociation efficiency of the blend. Deibel *et al.* [43] have estimated the carrier generation in polymer and fullerene blend by using Braun model and given the generation rate of free carriers as

$$G'(T,F) = G \times P(T,F) \tag{2.19}$$

where, *P* is the electric field dependent dissociation efficiency, which is given as

$$P(T,F) = \frac{k_d(F)}{k_d(F)+k_f} \tag{2.20}$$

with

$$k_d(F) = \frac{3e\mu}{4\pi\varepsilon a^3} e^{\left(-\frac{E_b}{k_b T}\right)} \frac{J_1\left(2\sqrt{-2b}\right)}{\sqrt{-2b}} \tag{2.21}$$

where, μ is the sum of electron and hole mobility, ε is the effective dielectric constant, a is the initial polaron-pair radius, E_b is the Coulombic binding energy, J_1 is the Bessel function of order 1 and $b = e^3F/8\pi\varepsilon(kT)^2$ and k_f is the geminate recombination rate.

As mentioned earlier, the Braun model has been used to compute the dissociation efficiency which is based on Onsager theory. However, Wojcik and Tachiya [44] have showed that there is a considerable difference between Braun model and the exact extension of Onsager theory.

Few other models for voltage dependent photocurrent can be found in the literature. Schilinsky *et al.* [45] proposed a model for photocurrent which is based on voltage depended mean carrier distance. The short circuit current density is multiplied by the ratio of average mean carrier distance to the total width of the active layer.

$$J_{ph}(V) = \begin{cases} -|J_{sc}|\ if\ \frac{\mu\tau(-V+V_{bi})}{W} > W \\ |J_{sc}|\ if\ \frac{\mu\tau(V+V_{bi})}{W} > W \\ |J_{sc}| \times \frac{\mu\tau(-V+V_{bi})}{W^2}\ \ else \end{cases} \tag{2.22}$$

However, this model does not consider direct recombination of photo-carriers and also fails to explain the dissociation of bound EHPs. Moreover, the internal quantum efficiency is assumed to be 100% while calculating the J_{sc}, whereas a lot of carriers undergo geminate recombination.

2.6 Summary

Physical structures of both BHJ solar cell (P3HT:PCBM) and thin-film solar cell (CdS/CdTe) have been discussed in this chapter. The analytical and numerical (Medici simulation) models are based on these structures. The properties and functions of the materials used in organic and inorganic solar cells have also been discussed. The various means of characterizing solar cell behavior is elaborately discussed. This chapter also includes brief discussion on the existing models for *J-V* characteristics.

CHAPTER 3

Numerical Model of Thin-Film CdS/CdTe Solar Cell

3.1 Introduction

Numerical analysis of device behavior has greatly contributed to our understanding of the characteristics of solar cell [19]. The complex device models, which are difficult to solve analytically, can easily be solved by numerical methods. To some extent, numerical analysis can provide more accurate solutions without numerous assumptions. Many important physical effects, which are essential for more precise modeling, can also be taken into account with the help of numerical analyses tools. Therefore, the numerical simulators have become an indispensable tool for modeling solar cell characteristics.

In this chapter, numerical analysis of the behavior of thin-film CdTe solar cell is performed using CADtool Medici© from Synopsys [46]. The numerical model is then validated by comparing with the experimental results in the literature. The effects of various parameters on the characteristics of thin-film CdTe solar cell have also been shown.

3.2 Introduction to Medici

The electric field inside the device is computed using Poisson's equation. Along with other physical equations, Medici solves the Poisson's equation numerically [46]

$$\nabla^2\varphi = -\nabla.E = \frac{e(p-N_a^- -n+N_d^+)}{\varepsilon} \quad (3.1)$$

Where, φ is the intrinsic Fermi potential, E is the built-in electric field and ρ is the charge density. N_a^- and N_d^+ are ionized acceptor and donor concentrations, respectively, e is the electron charge, p and n are hole and electron concentrations, respectively, and ε is the permittivity. The carrier profile is computed by continuity equations (Eq. 3.2 and 3.3). Therefore these equations also have impacts on the built-in electric field.

$$\frac{\partial p}{\partial t} = \frac{1}{e}\vec{\nabla}.\overrightarrow{J_n} - (r_n - g_n) \quad (3.2)$$

$$\frac{\partial n}{\partial t} = -\frac{1}{e}\vec{\nabla}.\overrightarrow{J_p} - (r_p - g_p) \quad (3.3)$$

In the equations above, r and g are the recombination and generation rates, respectively. The electron and hole current densities can be obtained by Boltzmann transport theory. Considering both drift and diffusion components, the current densities for electrons and holes can be expressed by

$$\overrightarrow{J_n} = e\mu_n\overrightarrow{E_n}n + eD_n\vec{\nabla}n \quad (3.4)$$

$$\overrightarrow{J_p} = e\mu_p\overrightarrow{E_p}p - eD_p\vec{\nabla}p \quad (3.5)$$

In order to predict more precise output, it is vital to incorporate series resistance in a solar cell. Since it is not possible to directly assign a value as series resistance in Medici, contact resistance has been used as series resistance. Medici is a two dimensional device simulator [46]. It computes the output considering the *xy*-plane. So, the unit of the output current density is A/μm. The unit of the current density has been converted to mA/cm^2 assuming that the results are identical along the *z* plane.

3.3 Device structure and parameters

The physical structure of thin-film CdTe solar cell is designed in Medici according to Fig. 2.1 (in Section 2.1.1). The thicknesses of the electrodes have been assumed to be zero in order to utilize the nodes more efficiently inside the device. It does not affect the output because, in practical thin-film CdTe solar cells, the front contacts are connected in grid and their area compared to the shining surface of the cell is negligible. In fact, a loss factor is used to take this loss along with other losses into account. The other losses are comprised of incomplete EHP generation, shading from the grid and photon absorption in the oxide layer [47]. The bottom electrode has been placed under the CdTe layer. The reflectance of the bottom contact is assumed to be 0.9. The various physical parameters used in the numerical simulation are listed in Table 3.1.

Table 3.1 Physical parameters used in numerical simulation

parameters	CdS	CdTe
Relative dielectric permittivity	9	9.4
Band-gap at 300 K (eV)	2.42	1.45
Electron affinity (V)	4.44	4.28
Effective density of states in the conduction band at 300 K (#/cm^3)	1.80×10^{19}	7.50×10^{17}
Effective density of states in the valence band at 300 K (#/cm^3)	2.40×10^{18}	1.80×10^{19}
Electron mobility (cm^2/V-s)	100	180
Hole mobility (cm^2/V-s)	20	20

3.4 Light source

The properties of a light source can be specified by Medici. A monochromic light source has been placed outside the solar cell. The built-in solar spectrum in Medici is similar to Air Mass Zero (AM 0) spectrum. However, in order to create a more realistic environment, the intensities of different wavelengths of incident photons have been manually specified which is similar to AM1.5 spectrum (ASTM G-173-03 standard) [48]. Figure 3.1 shows the sun spectrum at AM 1.5. Intensities of wavelengths from 0.3 μm to 0.9 μm has been considered for CdTe solar cells. The light beam strikes on the top surface of the solar cell with an incident angle of 90°.

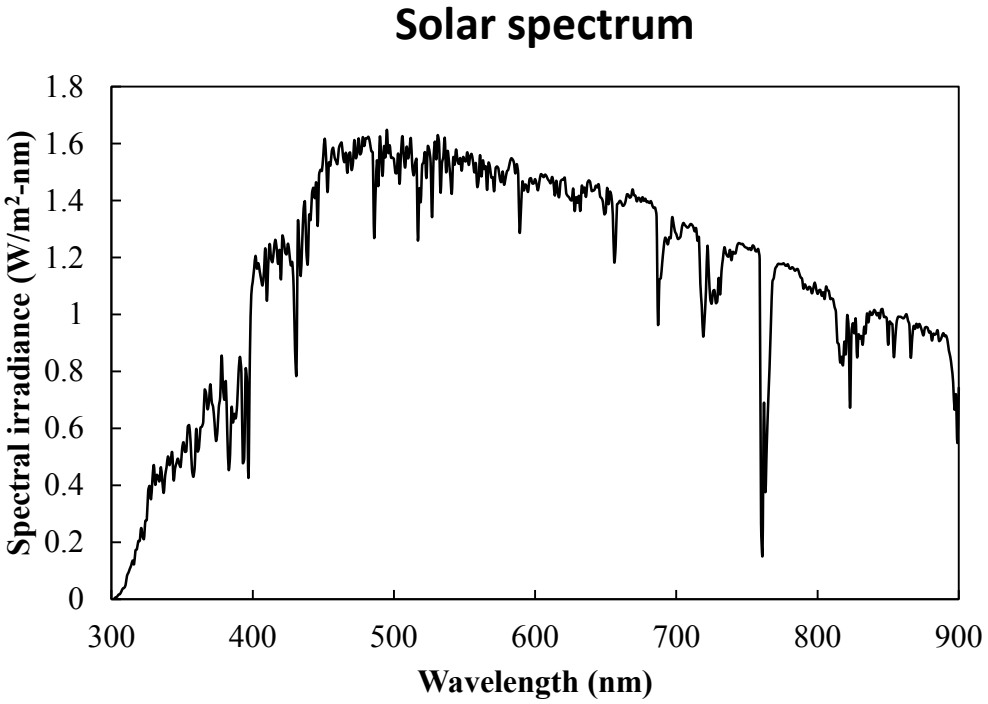

Figure 3.1 Sun spectrum at AM 1.5 (ASTM G-173-03 standard)

3.5 Photon absorption

Each wavelength of incident photons has a monochrome component of the light intensity which has been defined to make the solar light spectrum nearly identical to AM 1.5. There are losses in photo-generation due to reflection of light at the surface and interfaces. In order to include these losses, reflective indices of CdS and CdTe have been taken into account. The absorption coefficients of CdS and CdTe are also not defined in Medici. Therefore the absorption coefficients for different wavelengths have been manually specified.

3.6 Simulation results and conclusions

The simulation results in this chapter are obtained using Medici. The whole structure of a solar cell is divided into triangular simulation grids and then physical equations (i.e. Poisson's equation, current-continuity equations and transport equations) are simultaneously solved.

3.6.1 Photo carrier generation

Figure 3.2 illustrates the photo-generation rate along the window and absorber layer. The width of the window layer is kept fixed at 0.1 μm and the absorber layer is 3.5 μm.

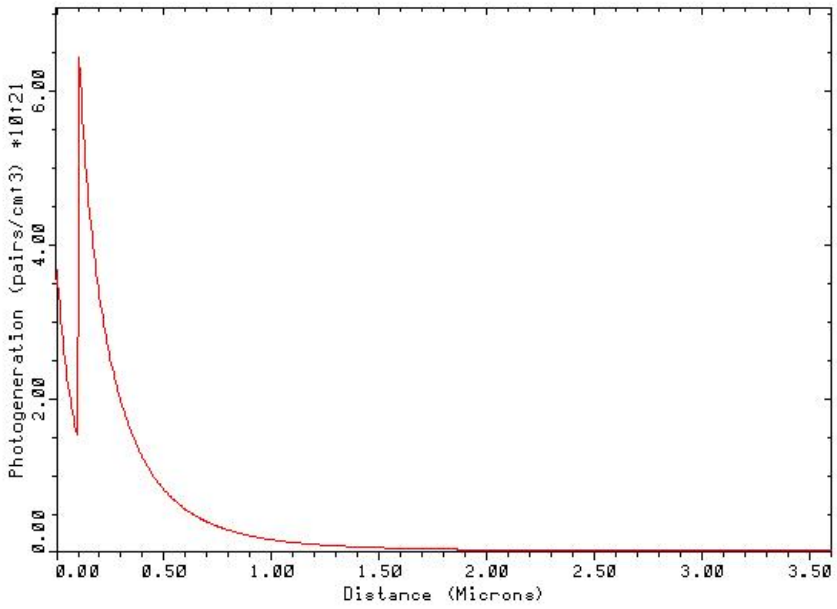

Figure 3.2 Total photo-carrier generation (EHPs) per cubic centimeter per second across the window and absorber layer

The high absorption coefficient of CdTe allows the absorber layer to absorb most of the photons within a width of ~2 μm. The high absorption coefficient reduces the penetration depth ($\delta=1/\alpha$) of the incident photons [49].

3.6.2 Energy band diagram

To get confidence and insights on device operation, the energy band diagrams at zero output voltage of a 1.1 μm thick CdTe layer solar cell under dark and illuminated conditions are shown in Figs 3.3a and 3.3b, respectively. The effects of back contact are also illustrated for dark (Fig 3.3c) and illuminated (Fig 3.3d) conditions. The doping concentrations in CdS and CdTe layers are 10^{18} and 10^{14} cm^{-3}, respectively. The energy band discontinuities at the interfaces are determined by the electron affinity of both materials. The reported values are quite scattered in the literature. The common values of electron affinity of polycrystalline CdS and CdTe are given in Table 3.1. There is a cliff of ~0.1 eV in the conduction band at the CdS/CdTe interface [50]. The cliff in the conduction band reduces the open circuit voltage. The magnitude of the cliff can be as high as ~0.2 eV, depending on the scattered values of electron affinity of two materials, which is still quite small for affecting carrier transport and open circuit voltage.

In Fig. 3.3a and 3.3b, the back electrode is Cu coated Au, which reduces the hole barrier at the back contact [17-18]. The quasi-Fermi level for holes near the back contact is quite flat in Fig. 3.3b, which shows a negligible hole barrier. The work function of the back contact has been increased (~5.5 eV) to reduce the hole barrier. However, the holes face an obstacle at the back contact if there is a Schottky barrier present between CdTe and

back electrode. The exact hole barrier height depends on the electron affinity of CdTe and the work function of the metal electrode. In this simulation, the back electrode is assumed to be Au with a work function of 5.1 eV (without Cu coating) to observe the back contact effects. The formation of hole barrier due to band bending near the back contact (as shown in Figs. 3.3c and 3.3d) can reduce the photocurrent in principle. The quasi-Fermi level for holes near the back contact in Fig. 3.3d shows accumulation of holes. Carrier generation due to illumination can be extracted from the potential difference between Fermi and quasi-Fermi levels of Fig. 3.3.

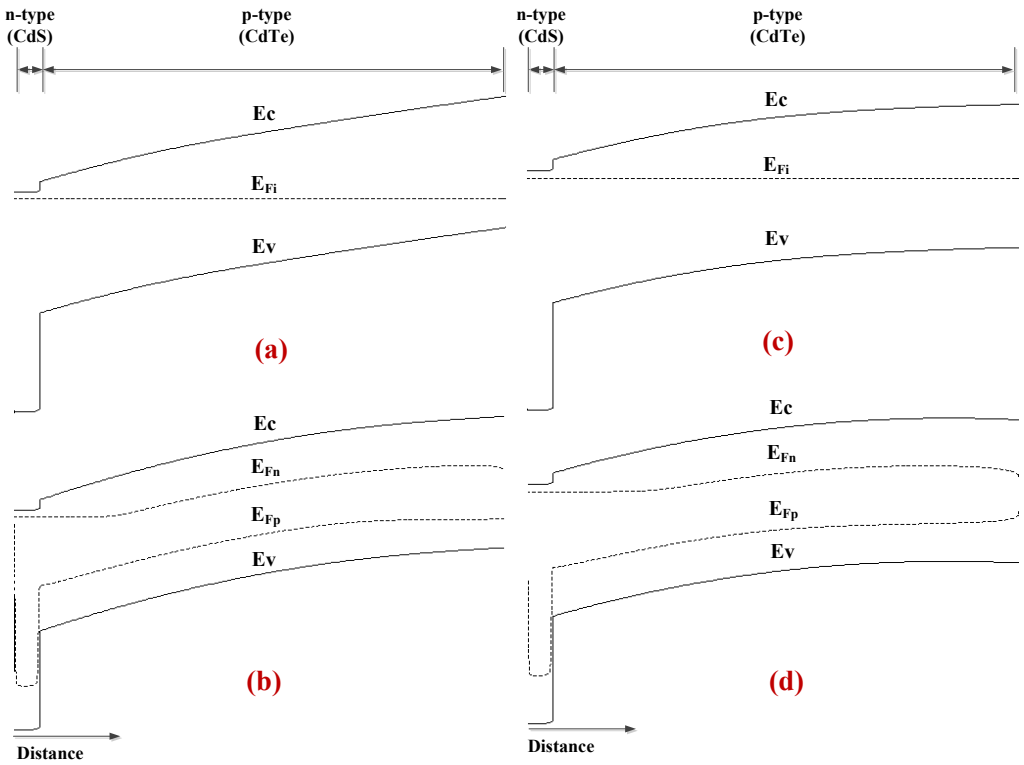

Figure 3.3 Energy band diagram of CdS/CdTe solar cell at different conditions, (a) dark and (b) illuminated condition without back contact effects and (c) dark and (d) illuminated condition with back contact effects.

3.6.3 Built-in electric field profile

Medici uses the Poisson's equation to calculate the built-in electric field. Figure 3.4 illustrates the electric field profile in the cell for different output voltages. The field has been calculated while the cell is illuminated.

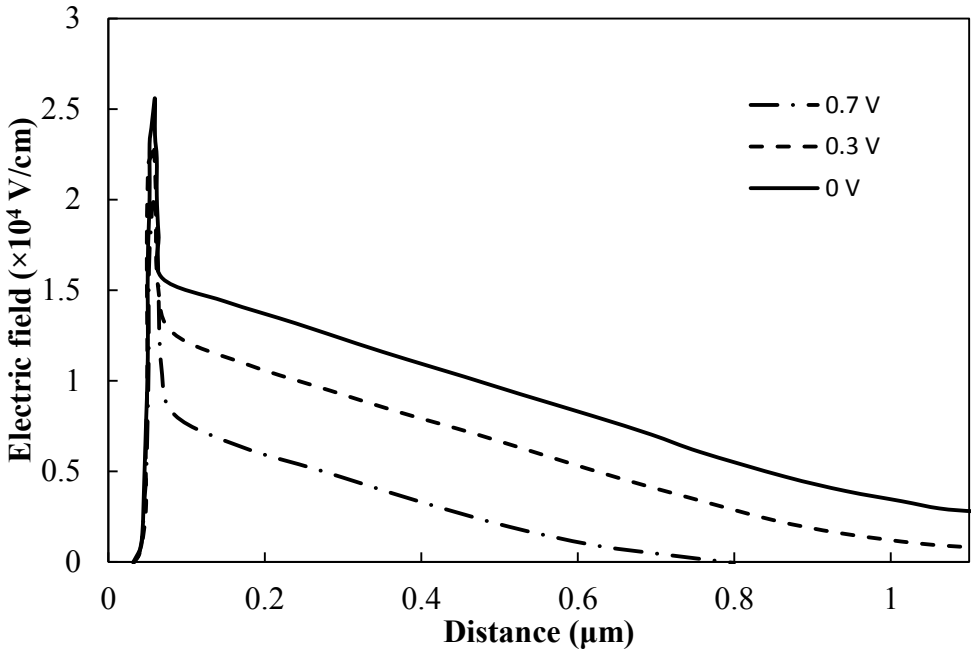

Figure 3.4 Built-in electric field profiles for different output voltages

The background doping and width of the absorber layer have been kept fixed at 10^{14} cm^{-3} and 1.1 μm, respectively. The width of the CdS is 0.06 μm. The built-in electric field mainly exists in the depletion region [29]. The width of the depletion region decreases with the increment of the forward bias voltage. From Fig. 3.4 it is evident that for higher output voltages, the absorber layer is partially depleted. Therefore, both electron and hole drift in the depleted region and diffuse in the field free region.

3.6.4 Carrier profile

Figure 3.5 illustrates electron and hole profiles across the window and absorber layers under dark condition. The widths of the absorber and window layers are 1.1 and 0.06 μm, respectively. The solar cell is in short circuit mode (voltage = 0V). Since there is no carrier generation in the device, minority carrier (electrons) in the absorber layer decreases along the width.

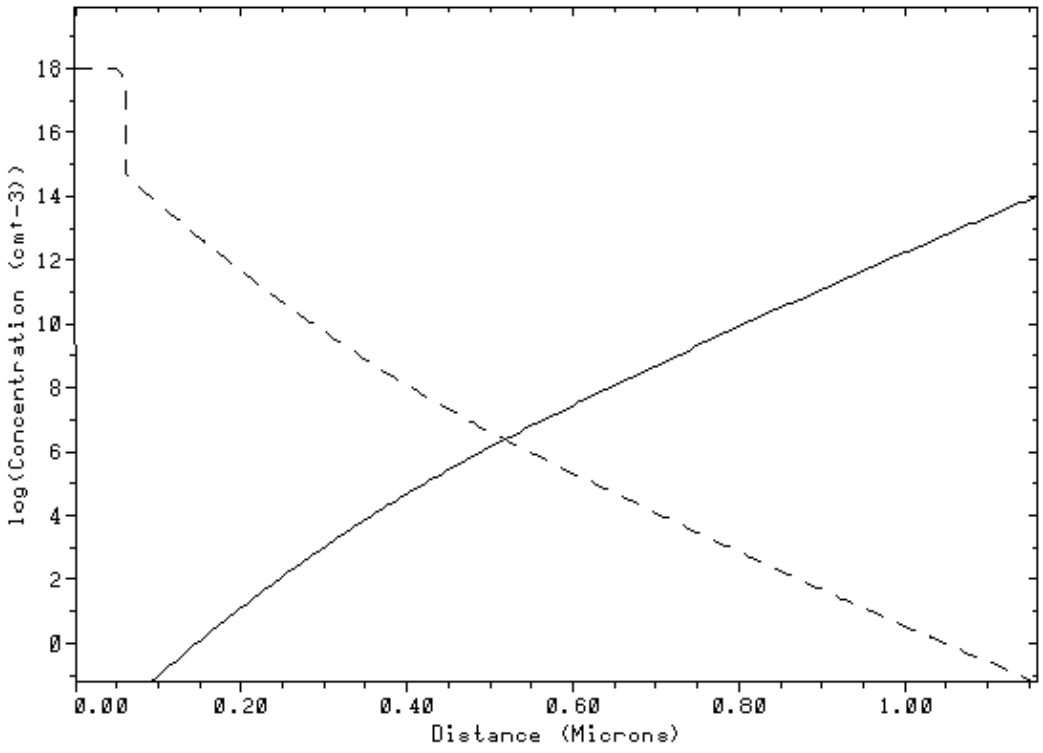

Figure 3.5 Electron (dashed line) and hole (solid line) profile across the window and absorber layers under dark condition

The carrier profiles change under illumination. Figure 3.6 shows the changes in carrier profile when the cell is exposed under the sun.

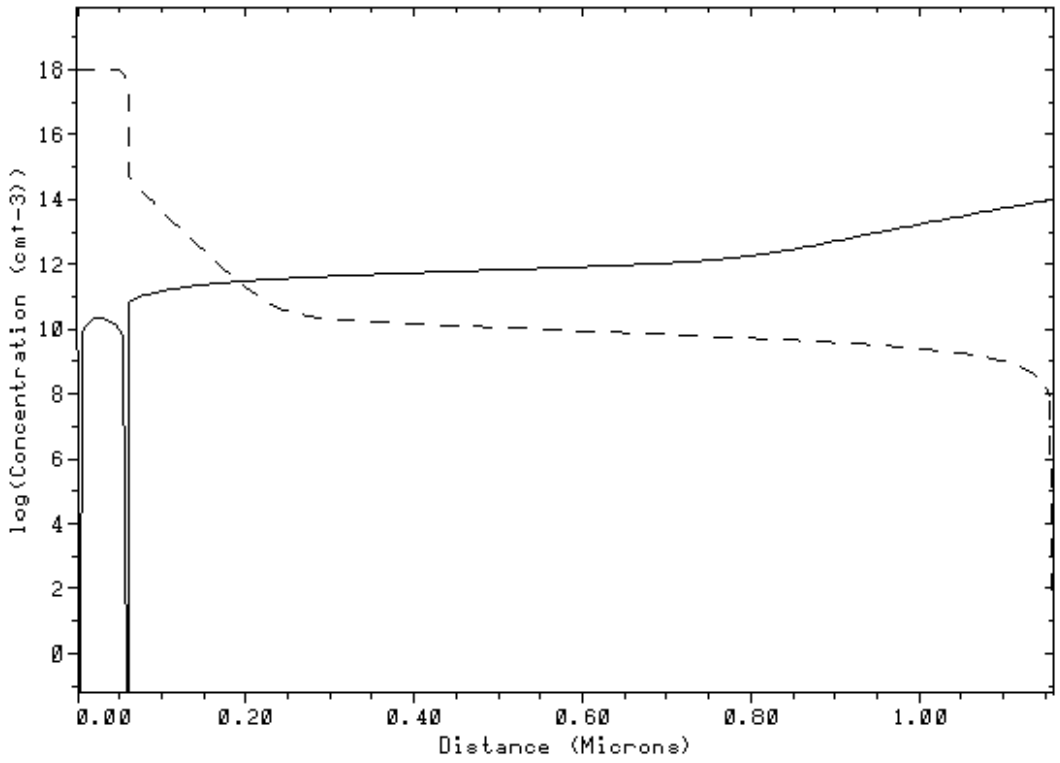

Figure 3.6 Electron (dashed line) and hole (solid line) profile across the window and absorber layers under illumination

3.6.5 Experimental fitting

The experimental results (Fig. 6 of Ref. [20]) are reconstructed to validate the numerical model and its outputs. In order to ensure the best fit to the experimental results, the values of various parameters (i.e. carrier life time, mobility, doping concentration, etc) have been chosen by trial and error. The absorber layer width is kept fixed at 3.5 μm. The values of the other parameters have been kept in close proximity to the reference data for CdS and CdTe [30]. Table 3.2 shows the values chosen for the best fit. Figure 3.7 shows that the experimental and simulated *J-V* curves are in good agreement.

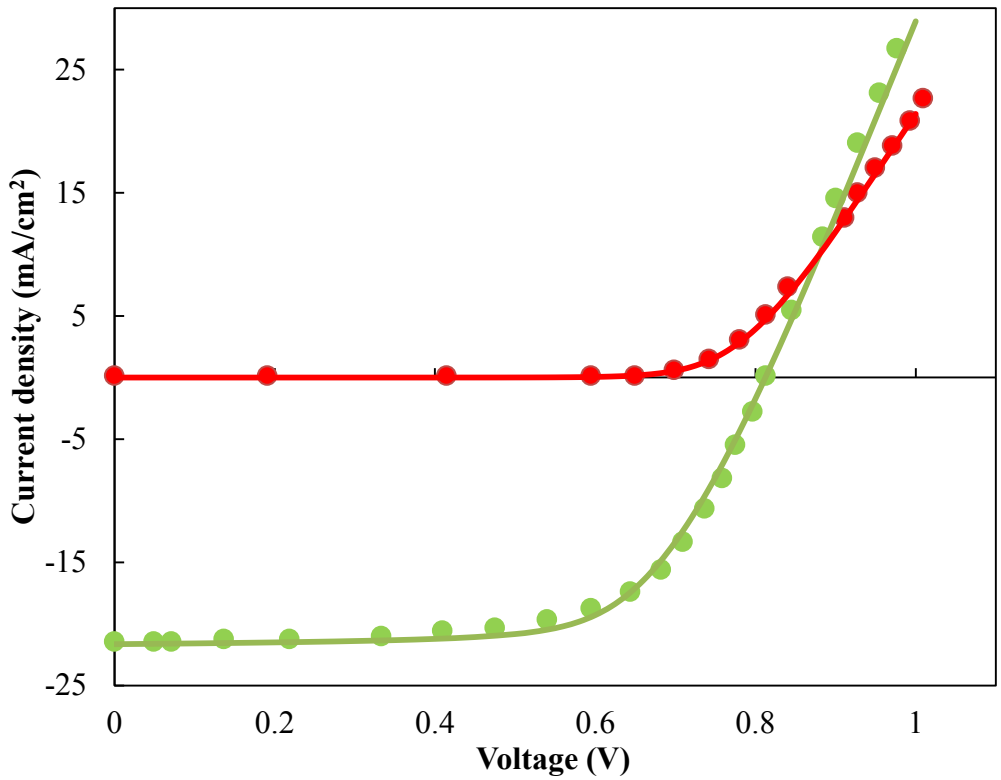

Figure 3.7 Symbols represent the experimental data for light (green) and dark (red) current densities, respectively. Solid lines represent the simulation results of light (green) and dark (red) current densities

Table 3.2 The values of the parameters to fit the experimental result

Parameters	CdS	CdTe
Hole lifetime (s)	10^{-10}	0.2×10^{-6}
Electron lifetime (s)	10^{-6}	7×10^{-9}
Doping concentration (cm^{-3})	10^{18}	10^{14}
Hole mobility (cm^2/V-s)	20	20
Electron mobility (cm^2/V-s)	100	180
Layer width (μm)	0.06	3.5

3.6.6 Effect of window layer width

Since all the photo-generated carriers in CdS layer are lost due to poor charge collection efficiency, it is necessary to minimize photon absorption in this layer [21,51]. The bandgap of CdS is ~2.45 eV. Thus photons up to 500 nm can be absorbed by CdS layer which is equivalent to ~7 mA/cm^2 if the maximum theoretical J_{sc} is assumed to be approximately 30 mA/cm^2 [51]. However, to minimize this absorption, the bandgap of CdS needs to be increased or the width has to be reduced [52]. The bandgap can be increased by using alloyed CdS [51]. The effect of CdS layer width on the *J-V* characteristics is illustrated in Fig. 3.8.

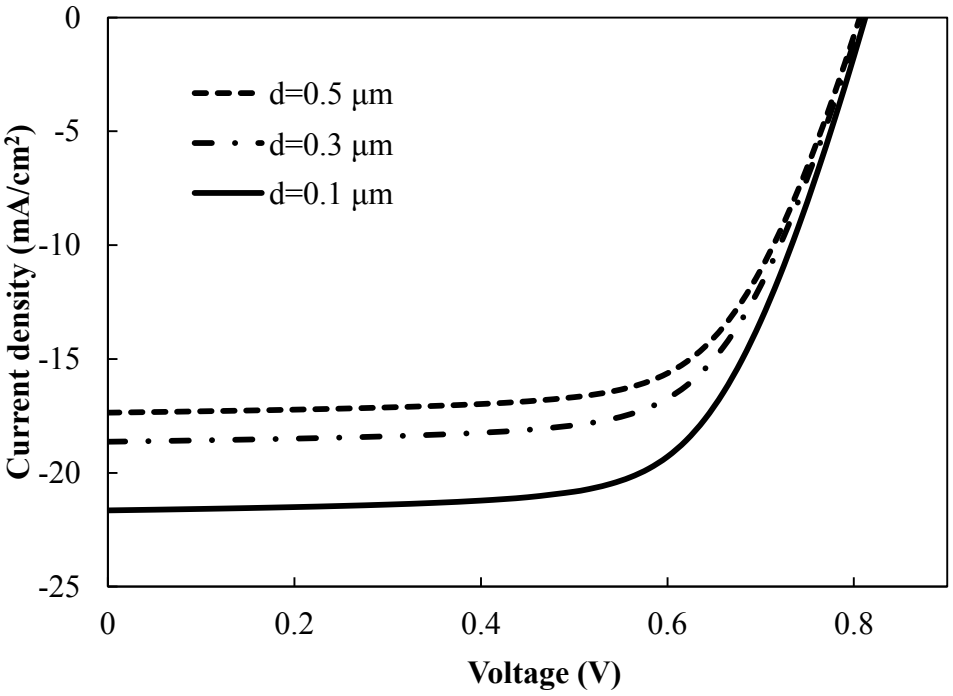

Figure 3.8 *J-V* curves for different widths of CdS layer

As expected, reducing of CdS layer thickness increases the J_{sc}. Increased photons absorption in CdTe layer is responsible for this enhancement of $J_{sc.}$

3.7 Summary

In this chapter, numerical modeling of thin-film CdS/CdTe solar cell is performed using device simulator tool, Medici. The numerical model has shown good agreement with the experimental results. The band diagrams, photon absorption, carrier profiles and electric field profiles at various conditions that have been illustrated, provided a better insight into device physics of a CdS/CdTe solar cell. The effect of window layer width on *J-V* curve has also been presented.

CHAPTER 4

Modeling of the Effects of Charge Transport on Voltage-Dependent Photo-Current in Ultra-Thin CdTe Solar Cells

The contribution of this chapter has recently been published [53]. Most of the materials are taken from Ref. [53].

4.1 Abstract

An analytical model is developed to study the current-voltage characteristics of CdTe thin film solar cells by incorporating exponential photon absorption, carrier trapping, carrier drift and diffusion in the photon absorber layer. An analytical expression for the external voltage-dependent photocurrent is derived considering partial depletion of the absorber layer at operating terminal voltage. The overall load current is calculated considering the actual solar spectrum and dark current components. The analytical model is verified by Taurus Medici simulation and published experimental results for different absorber layer thicknesses. A good agreement of the analytical and numerical models with experimental data is ensured by reducing carrier lifetimes in the thinner absorber layers. The hole lifetime is reduced drastically by decreasing the width of the absorber thickness from 1.1 μm to 0.5 μm and the cell efficiency depends critically on the transport properties of the holes. The results of this paper indicate that the improvement of the charge transport

properties in submicron CdTe solar cells is extremely important to increase the power conversion efficiency.

4.2 Introduction

The structure of CdTe solar cell has already been shown in Fig. 2.1 (chapter 2). The photons are mainly absorbed in the CdTe layer and create free electron-hole pairs (EHPs) there. The photo-generated EHPs are collected by the built-in electric field. The voltage dependent charge collection in the depleted absorber layer is the dominant charge collection mechanisms [19, 21]. The absorber layer is partially depleted at operating (relatively high) output voltage as depicted in Fig. 4.1b. The thermal equilibrium concentration of charge carriers (~2.5 $\times 10^{6}$ cm^{-3}) is negligibly small because of high bandgap (1.45 eV in CdTe). Therefore, charge neutrality may not exist outside of the depletion region of the CdTe layer (CdTe is usually treated as a photoconductor rather than a conventional semiconductor). However, the electric field in the outside of depletion region is negligible as compared to the depletion region because the photo-generated excess charge carrier concentrations (~10^{11} to 10^{12} cm^{-3} for normal sun intensity) are much smaller compared to the doping concentration (~10^{14} cm^{-3}). As a consequence, the charge carriers move mainly by drift and diffusion mechanisms in the depletion and outside of the depletion (field-free) regions, respectively.

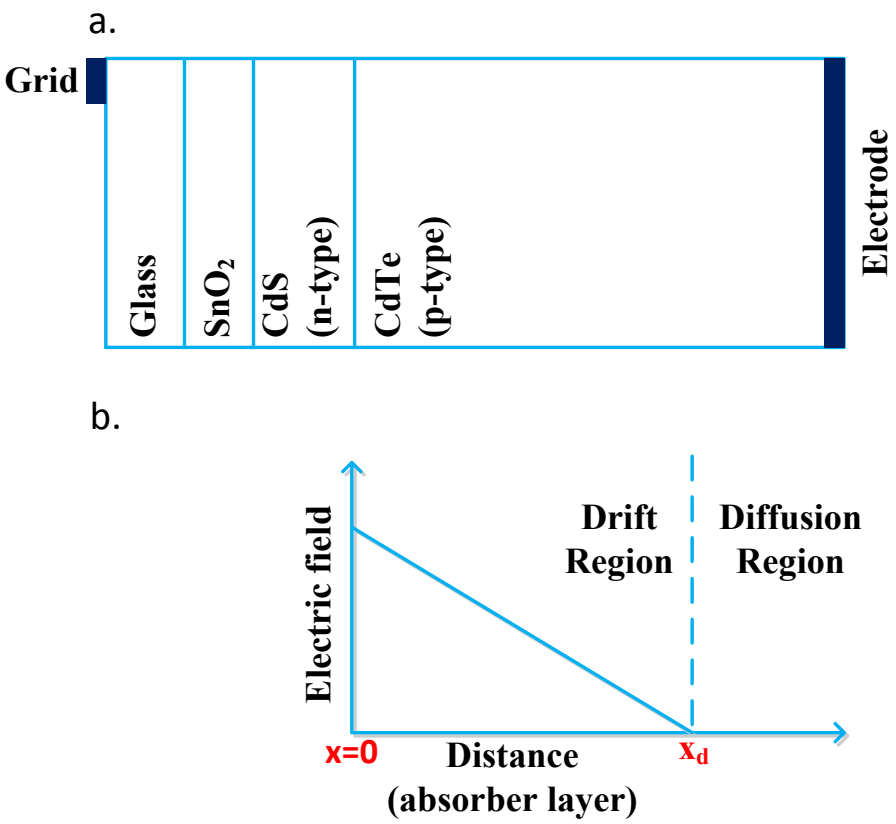

Figure 4.1 (a) The structure of a CdTe/CdS solar cell (not in scale), and (b) electric field profile in the CdTe absorber layer at higher output voltage

In this chapter, an analytical model for voltage-dependent photocurrent has been proposed considering both electron and hole drift in the depleted region and diffusion in the field free region by solving continuity equations with proper boundary conditions. Exponential photon absorption and actual solar spectrum are considered to compute the photocurrent densities at entire output voltages. The incident photon flux is taken as the air mass (AM) 1.5 global spectra from the ASTM G-173-03 standard [48]. The overall load current is computed considering the effect of voltage-dependent forward dark current which consists of recombination current in the depleted region and the diffusion current in the field-free region. The results of the analytical model are verified by the 2D Taurus Medici device simulator. The model is also compared with the recently published

experimental results on ultra-thin CdTe solar cells in order to determine the carrier transport properties (defects and carrier lifetimes) and effective doping concentrations.

4.3 Analytical model

As mentioned earlier, the charge carriers move by drift and diffusion mechanisms in the depleted and field-free regions, respectively. The electric field profile is triangular for the uniformly distributed space charges in the depleted region as shown in Fig. 4.1b. In the depleted region electrons drift towards the illuminated surface (front contact) and holes drift towards the bottom metal contact (back contact). The drift velocity of the photo-generated carriers is higher near the CdTe/CdS interface compared to that at near the field-free region [21]. Therefore, considering an average drift velocity of the carriers throughout the absorber layer will not impact the output significantly.

Few assumptions are made to develop an analytical model for the *J-V* characteristics.

(1) The built-in electric field is uniform in the depleted portion of the absorber layer.

(2) Due to the large bandgap of the materials, the thermal equilibrium charge carriers concentration is considered to be negligible.

(3) The diffusion of charge carriers is negligible compared to carrier drift in the depletion region.

(4) The mobility (μ) and lifetime (τ) of the carriers (electrons and holes) are assumed to be constant throughout the whole absorber layer.

4.3.1 Net external current density

The net external current density from a solar cell is [54]

$$J(V) = J_d(V) + \frac{V - JR_s}{R_p} - J_{ph}(V), \tag{4.1}$$

where V is the output voltage, J_{ph} is the photocurrent density, R_s is the series resistance, R_p is the shunt resistance and J_d is the forward diode current density.

4.3.2 Dark current density

The forward dark current consists of recombination current in the depleted region and the diffusion current in the field-free region. Thus the expression of J_d can be given as [54,55,56],

$$J_d = \begin{cases} \left(\frac{en_i x_d V_t \pi}{2\sqrt{\tau_n \tau_p}\{V_{bi} - V\}}\right) e^{\frac{V - JR_S}{2V_t}} + \left(\frac{eD_n n_i^2}{L_n N_a}\right) e^{\frac{V - JR_S}{V_t}} \; ; x_d < W \\ \left(\frac{en_i W V_t \pi}{2\sqrt{\tau_n \tau_p}\{V_{bi} - V\}}\right) e^{\frac{V - JR_S}{2V_t}} \; ; \; x_d \geq W \end{cases}, \tag{4.2}$$

Where, $x_d = \sqrt{\frac{2\varepsilon[V_{bi} - (V - JR_s)]}{eN_a}}$; $x_d < W$ (4.3)

$= W$ otherwise.

and $L_n = \sqrt{\tau_n D_n}$ is the electron diffusion length.

Here e is the elementary charge, n_i is the intrinsic carrier concentration of CdTe, $V_t \left(= \frac{k_b T}{e}\right)$ is the thermal velocity, k_b is the Boltzmann constant, T is the absolute temperature, x_d is the width of the depletion region, W is the width of the CdTe layer, V_{bi} is the built in potential voltage between the n-type and p-type layers, D is the diffusion coefficient, N_a and ε are the doping concentration and the permittivity of the absorber layer respectively. The subscript n and p represent electrons and holes, respectively.

4.3.3 EHP generation

The photon absorption in the highly doped CdS n-layer contributes a negligible current because of their very short diffusion length and the extremely thin width of CdS [57]. The photons are mainly absorbed in the CdTe absorber layer. The electron-hole pair generation rate G in the absorber layer can be written as [21],

$$G(\lambda) = \alpha(\lambda) e^{-\alpha_1 d} [1 - R(\lambda)] \lambda I_o(\lambda) / hc \tag{4.4}$$

where I_o is the intensity of the solar spectra (W/cm^2-nm), c is the speed of light, h is the Planck constant, R is the reflection, scattering, and other loss factors, $\alpha(\lambda)$ is the absorption coefficient of the absorber layer, λ is the incident photon wavelength, α_1 and d are the absorption coefficient and width of the CdS window layer, respectively. Shading from the grid, incomplete EHP generation in the absorber layer and photon absorption in the oxide layer contribute to the other losses [47].

4.3.4 Voltage-dependent Photocurrent

The photo current in the photovoltaic structures can be written as,

$$J_{ph}(\lambda, V) = J_n'(\lambda, V, x) + J_p'(\lambda, V, x) + J_D'(\lambda, V, x) \quad (4.5)$$

Where, $J_D'(\lambda, V, x)$ is the displacement current density, $J_n'(\lambda, V, x)$ and $J_p'(\lambda, V, x)$ are the conduction current densities for electrons and holes, respectively. The conduction current density consists of both drift and diffusion currents. Considering the spatial invariant property of the total photocurrent, the expression of the photocurrent density for a fixed voltage can alternately be written as [58],

$$J_{ph}(\lambda, V) = \frac{1}{W}\int_0^W \left\{J_n'(\lambda, V, x) + J_p'(\lambda, V, x)\right\} dx = J_n(\lambda, V) + J_p(\lambda, V) \quad (4.6)$$

The conduction currents for holes and electrons are determined by the excess carrier concentrations due to irradiation. The excess carrier concentrations for both holes and electrons across the CdTe layer are calculated by solving the continuity equations. Since charge neutrality may not exist in the outside of the depletion region, the continuity equations for both holes and electrons are solved separately. Thus the conduction currents for both holes and electrons will be determined separately using the excess carrier profiles.

Considering the assumptions mentioned above (Section 4.3), the steady-state continuity equation for holes is,

$$\frac{\partial}{\partial t}(\delta p) = -\mu_p F \frac{\partial}{\partial x}(\delta p) + D_p \frac{\partial^2}{\partial x^2}(\delta p) + G e^{-\alpha(\lambda)x} - \frac{\delta p}{\tau_p} = 0 \quad (4.7)$$

where δp is photo generated hole concentration, x is the distance along the absorber layer from the CdS/CdTe interface and G is the EHP generation rate at $x = 0$. Here subscript p represents holes. Due to the built-in field in the depletion region, photo-generated holes immediately start drifting towards the back contact ($i.e., \delta p = 0$ at $x = 0$) and recombine with a velocity of S_p (surface velocity) at the back contact.

$$S_p \delta_p = -D_p \frac{\partial \delta p}{\partial x} \tag{4.8}$$

Thus the solution of Eq. (4.7) is,

$$\delta_p(x,\lambda) = \begin{cases} \frac{G\tau_p}{(1-\mu_p \tau_p F\alpha)}\left[e^{-\alpha x} - e^{-\frac{x}{\mu_p \tau_p F}}\right], & x < x_d \\ M_1 cosh\left(\frac{x}{L_p}\right) + M_2 sinh\left(\frac{x}{L_p}\right) + \frac{G\tau_p e^{-\alpha x}}{(1-L_p^2\alpha^2)}, & x \geq x_d \end{cases} \tag{4.9}$$

Where,

$$M_1 = [Q - M_2 R], \tag{4.10}$$

$$M_2 = \left[\frac{P - Q cosh\frac{x_d}{L_p}}{sinh\frac{x_d}{L_p} - R cosh\frac{x_d}{L_p}}\right], \tag{4.11}$$

$$P = G\tau_p \left[\frac{e^{-\alpha x_d} - e^{-\frac{x_d}{\mu_p F \tau_p}}}{1-\alpha \mu_p F \tau_p} - \frac{e^{-\alpha x_d}}{1-L_p^2\alpha^2}\right], \tag{4.12}$$

$$Q = \frac{\left(\frac{G\tau_p}{1-L_p^2\alpha^2}\right)e^{-\alpha W}(D_p\alpha - S_p)}{S_p cosh\frac{W}{L_p} + \frac{D_p}{L_p} sinh\frac{W}{L_p}}, \tag{4.13}$$

$$R = \frac{S_p sinh\frac{W}{L_p} + \frac{D_p}{L_p} cosh\frac{W}{L_p}}{S_p cosh\frac{W}{L_p} + \frac{D_p}{L_p} sinh\frac{W}{L_p}} \quad , \tag{4.14}$$

and $L_p = \sqrt{D_p \tau_p}$ is the hole diffusion length.

The photo current density for the holes which are travelling towards the bottom contact is,

$$J_p(\lambda, V) = \frac{1}{W}\left\{\int_0^W J'_p(\lambda, V, x)dx\right\}$$

$$= \frac{e}{W}\left\{\mu_p F \int_0^{x_d} \delta p dx - D_p \int_{x_d}^{W} \frac{\partial \delta p}{\partial x} dx\right\}$$

$$= \frac{eG\tau_p \mu_p F}{W(1-\mu_p F \tau_p \alpha)}\left[\mu_p F \tau_p \left(e^{-\frac{x_d}{\mu_p F \tau_p}} - 1\right) - \frac{1}{\alpha}(e^{-\alpha x_d} - 1)\right]$$

$$-\frac{eD_p}{W}\left[M_1\left(cosh\frac{W}{L_p} - cosh\frac{x_d}{L_p}\right) + M_2\left(sinh\frac{W}{L_p} - sinh\frac{x_d}{L_p}\right) + \frac{G\tau_p}{1-L_p^2\alpha^2}(e^{-\alpha W} - e^{-\alpha x_d})\right] \tag{4.15}$$

Similarly, the excess electron concentration distribution is determined by solving the steady-state continuity equation for electrons in the depletion and field-free regions (considering $\delta n \approx 0$ at $x = x_d$) [21,56], and thus the electrons density is,

$$\delta_{n,}(x, \lambda) = \frac{G\tau_n}{(1+\alpha F \mu_n \tau_n)}\left[e^{-\alpha x} - e^{-x_p\left(\frac{1}{F\mu_n\tau_n} + \alpha\right) + \frac{x}{F\mu_n\tau_n}}\right]$$

$$+ M_1' cosh\left(\frac{x}{L_n}\right) + M_2' sinh\left(\frac{x}{L_n}\right) + Ae^{-\alpha x} \tag{4.16}$$

where

$$M_1' = \left[\frac{P'e^{-\alpha W}(D_n\alpha - S_n) - M_2'R'}{Q'}\right] \tag{4.17}$$

$$M_2' = \left[\frac{P'Q'e^{-\alpha x_p} + P'e^{-\alpha W}(D_n\alpha - S_n)cosh\left(\frac{x_p}{L_n}\right)}{R'cosh\left(\frac{x_p}{L_n}\right) - Q'sinh\left(\frac{x_p}{L_n}\right)}\right] \tag{4.18}$$

$$P' = \frac{G\tau_n}{1 - D_n\tau_n\alpha^2} \tag{4.19}$$

$$Q' = S_n cosh\left(\frac{W}{L_n}\right) + \frac{D_n}{L_n} sinh\left(\frac{W}{L_n}\right) \tag{4.20}$$

$$R' = S_n sinh\left(\frac{W}{L_n}\right) + \frac{D_n}{L_n} cosh\left(\frac{W}{L_n}\right) \tag{4.21}$$

The photo current density for the electrons which are travelling towards the front contact is,

$$J_n(\lambda, V) = \frac{e}{W}\left\{\mu_n F \int_0^{x_d} \delta n dx + D_n \int_{x_d}^{W} \frac{\partial \delta n}{\partial x} dx\right\}$$

$$= \frac{eG\tau_n\mu_n F}{w(1+\mu_n F\tau_n\alpha)}\left[\mu_n F\tau_n\left\{e^{-x_d\left(\frac{1}{F\mu_n\tau_n}+\alpha\right)} - e^{-x_d\left(\frac{1}{F\mu_n\tau_n}+\alpha\right)+\frac{x_d}{\mu_n F\tau_n}}\right\} - \frac{1}{\alpha}(e^{-\alpha x_d} - 1)\right] + \frac{eD_n}{W}\left[M_1'\left(cosh\frac{W}{L_n} - cosh\frac{x_d}{L_n}\right) + M_2'\left(sinh\frac{W}{L_n} - sinh\frac{x_d}{L_n}\right) + P'(e^{-\alpha W} - e^{-\alpha x_d})\right] \tag{4.22}$$

The total photo current density can be obtained by integrating over all incident photon wavelengths of the solar spectrum, i.e.

$$J_{ph}(V) = \int_0^{\infty} \{J_p(\lambda, V) + J_n(\lambda, V)\} d\lambda \quad (4.23)$$

4.3.5 Built-in electric field

The built-in electric field in the depletion region is a function of the output voltage and given as [20],

$$F(V) = \frac{V_0 - V_j}{x_d} = \frac{V_0 - (V - JR_s)}{x_d} \quad (4.24)$$

where V_j ($=V - JR_s$) is the junction voltage, and V_0 is the flat-band voltage. At $V_j = V_o$, the field becomes zero (see Eq. 4.24). From the existing theories of semiconductors, it is predicted that the electric field diminishes while the applied V_j is equal to the V_{bi}. However, several experiments reveal that the field reduces to zero just beyond V_{oc} and slightly less than V_{bi} [20]. Generally V_0 is around 0.1 V more than the V_{oc}. Therefore, V_0 is assumed to be a fitting parameter in this work.

4.4 Numerical model

As mentioned, 2D Taurus Medici is used for the numerical simulations [46]. For each simulation, the structure of the cell is redesigned according to the experimental details. The physical parameters used in the numerical simulation are already shown in Table 3.1. The solar intensity is defined in such way that solar light spectrum is almost identical to

AM1.5. The doping concentrations in CdS and CdTe layers are 10^{18} and 10^{14} cm^{-3}, respectively.

4.5 Results and discussions

4.5.1 Verification of the analytical model

The analytical model is verified by fitting with the published experimental data and Medici simulation. The analytical model has similar doping concentration and carrier mobility as the numerical model. Figure 4.2 shows the *J-V* curves of CdS/CdTe solar cells at three sun intensities (100, 32, and 10 % of 1.5 AM global spectrum). The symbols represent experimental data, the solid and dotted lines represent analytical and numerical (Medici simulation) results, respectively. The experimental data were extracted from Fig. 2 of Ref. [20]. The CdTe thickness is 1.8 μm. The CdS thickness is assumed as 0.2 μm. The best fit parameters for the analytical and numerical simulation are the same. The best fit lifetimes of holes and electrons are $\tau_h = 8\times10^{-7}$ s and $\tau_e = 2\times10^{-9}$ s, which are consistent with the lifetime values in electrodeposited CdTe [59-60]. The other fitted parameters in Fig. 4.2 are: $N_a = 1.3 \times 10^{14}$ cm^{-3} and $R_s = 6$ Ω-cm^2.

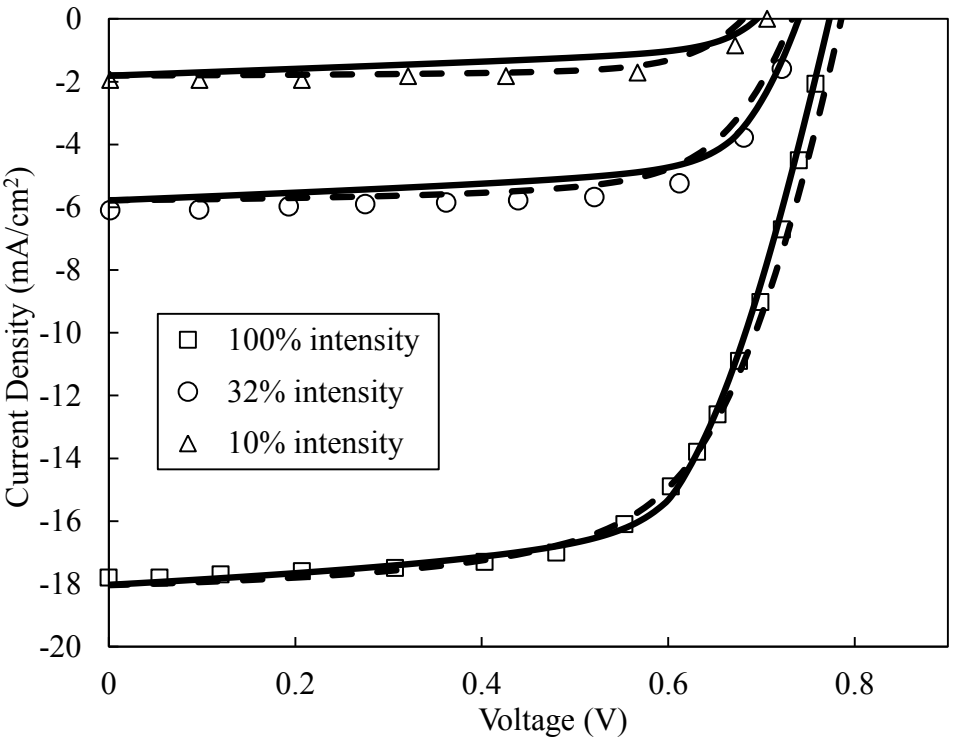

Figure 4.2 *J-V* curves for a CdTe/CdS solar cell for three different sun intensities. The experimental data are represented by the symbols and analytical and numerical results are represented by the solid and dotted lines, respectively

4.5.2 Toward ultra-thin absorber

Figure 4.3 shows the *J-V* curves of CdTe/CdS solar cells with different absorber layer thicknesses (i.e., 0.5, 0.65, 0.85 and 1.1 μm). The thickness of CdS layer is kept fix at 0.06 μm. The symbols represent experimental data, and the solid and dotted lines represent analytical and numerical (Medici simulation) results, respectively. The experimental data were extracted from Fig. 1 of Ref. [61]. The doping concentrations and carrier mobilities are mentioned in Section 4.4 and Table 3.1. The carrier lifetimes have been varied within an acceptable range to best fit the experimental values. It is to be noted that the lifetimes for both carriers used in the analytical and numerical models for

each thickness are the same, which are given in Table 4.1. The analytical model agrees well with the Medici simulation and experimental results.

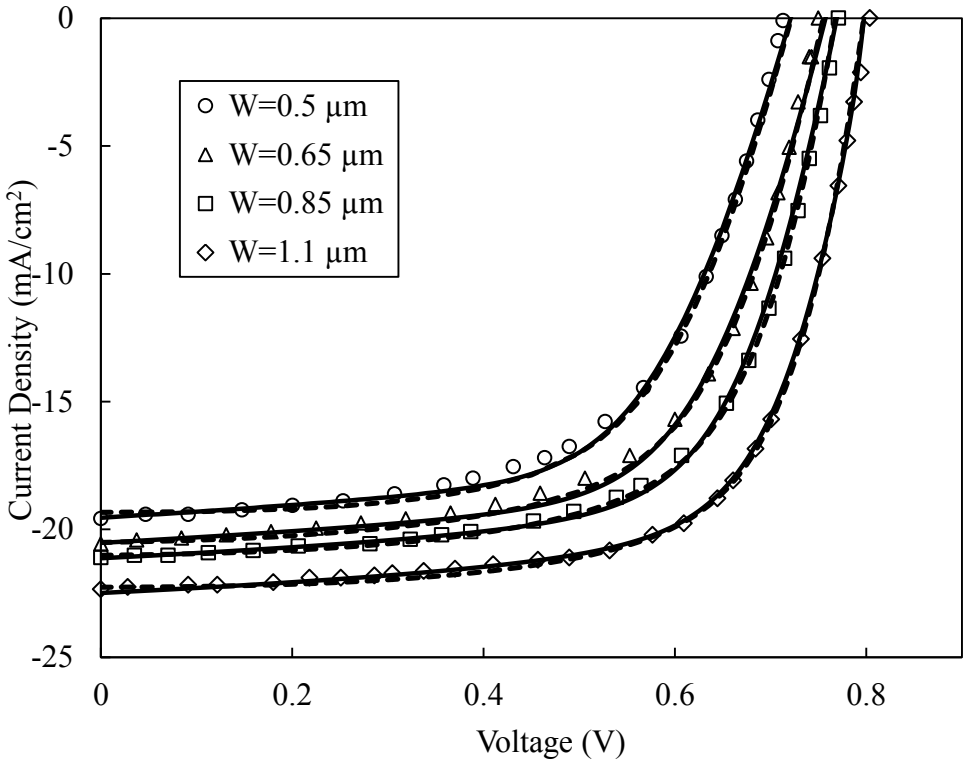

Figure 4.3 *J-V* curves for CdTe/CdS solar cells for different absorber layer thicknesses. Solid and dotted lines represent analytical and numerical results, respectively

The short circuit current, open circuit voltage, and fill factor all reduce with decreasing the CdTe thickness as evident from Fig. 4.3. The light absorption is obviously lower in thinner absorber layer. The light absorption is reduced by 6.3 % only as the absorber decreases from 1.1 μm to 0.5 μm, whereas, for the same reduction of the absorber layer, the short circuit current (J_{sc}) and the power conversion efficiency are reduced by ~12% and ~30%, respectively. The voltage-dependent carrier transport properties are responsible for this discrepancy. The hole lifetime decreases from 8×10^{-7} s to 2×10^{-9} s as

the width of the absorber layer reduces from 1.1 μm to 0.5 μm. Note that the fitted values of lifetimes mentioned above represent the average lifetime in the bulk.

Table 4.1 Best fitted parameters used in analytical and numerical models for different absorber layer widths.

W (μm)	τ_n (s)	τ_p (s)	R_s (Ω-cm^2)	R_p (Ω-cm^2)	Conversion efficiency (η)
0.5	1×10^{-10}	2×10^{-9}	5	600	8.48 %
0.65	1×10^{-10}	1×10^{-8}	4.1	600	9.76 %
0.85	1×10^{-10}	2×10^{-7}	2.9	820	10.58 %
1.1	1×10^{-10}	8×10^{-7}	2.1	980	11.92 %

In practice, the carrier lifetime near the back contact is usually much smaller (In fact, time-resolved photoluminescence as a function of depth can give experimental values of the space dependent lifetimes). Moreover, the interface defects can be treated as an equivalent defect states for the bulk in the theoretical model. Again, Cu can easily diffuse to the absorber layer from the back-contact in shorter devices and eventually acts as recombination centers [17]. The interface effects are more prominent in shorter devices, which can reduce the average carrier lifetime [17]. Lower carrier lifetimes in shorter devices result an increment of the leakage current and reduction of photocurrent, which in turn reduces the V_{oc} and FF, and hence reduces the power conversion efficiency. The increase of series resistance in shorter devices due to weakly formed interfaces and contacts also reduces the FF.

It is also observed in both models that R_p decreases from 980 Ω-cm^2 to 600 Ω-cm^2 when W reduces from 1.1 μm to 0.5 μm. Ultra-thin solar cells with small grains are prone to form shunt paths, which leads to the reduction of R_p and carrier lifetimes [17,61]. The formation of hole barrier due to band bending near the back contact can reduce the photocurrent in principle. The exact hole barrier height depends on the electron affinity of CdTe and the work function of the metal electrode. We believe that the very little hole barrier in the present cell shown in Fig. 3.3 has negligible effect on the hole transport or photocurrent.

4.5.3 Effects of carrier lifetime

Since the analytical model agrees well with the accurate numerical model, we use our analytical model to examine the effects of carrier lifetimes and doping concentration on the *J-V* characteristics. The effects of hole (τ_p) and electron (τ_n) lifetimes for the W = 0.5 μm cell are shown in Figs. 4.4 and 4.5, respectively.

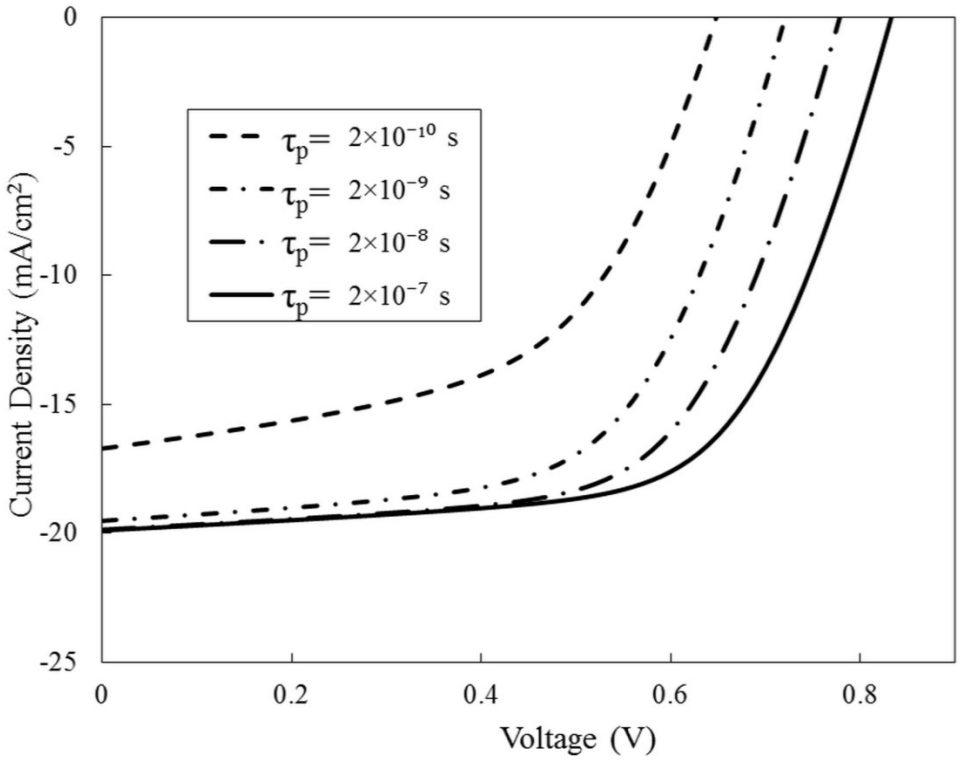

Figure 4.4 Net current density versus output voltage for various hole lifetimes for W = 0.5 μm and $\tau_n = 10^{-10}$ s.

It is evident that the cell performance mainly depends on hole transport properties. The theoretical overall efficiency of the cell decreases from 10.64 % to 5.84% when the hole lifetime is reduced from 2×10^{-7} s to 2×10^{-10} s whereas, for the same variation of electron lifetime, the efficiency decreases from 11.14% to 8.54%. It is because the electron and hole pairs are mainly generated in the vicinity of the CdS/CdTe interface due to high absorption coefficient of the absorber layer up to the wavelength of 900 nm. Photo-generated electrons quickly move towards the thin CdS layer whereas holes have to travel a longer distance in the CdTe layer. Therefore, the charge collection efficiency is mainly controlled by the hole transport.

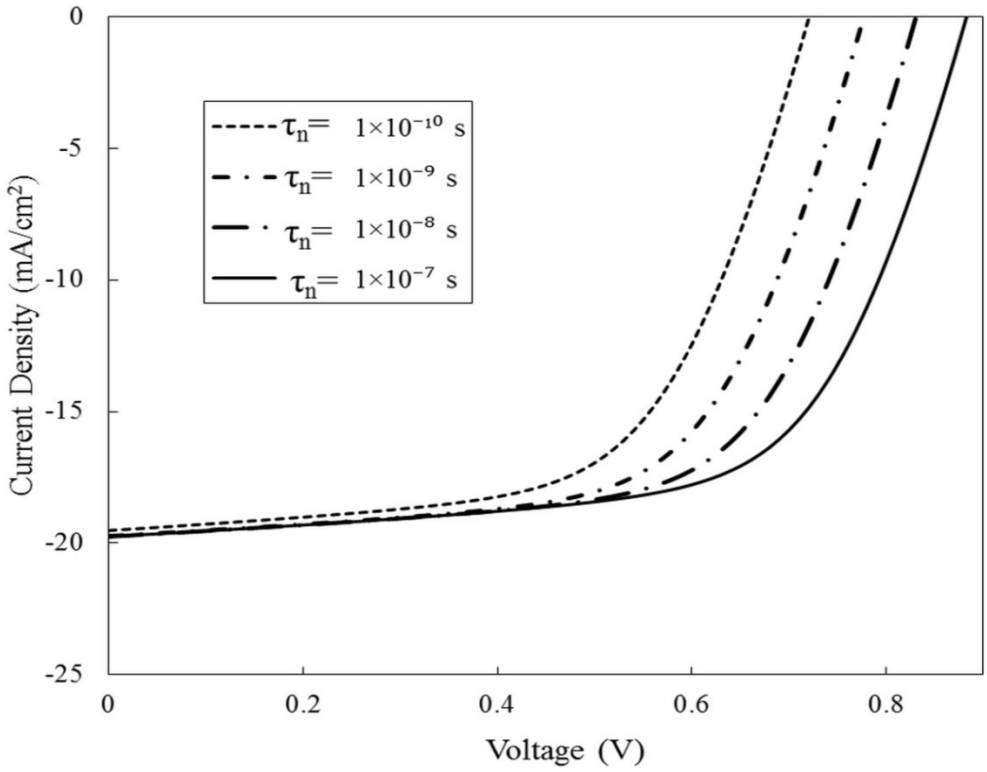

Figure 4.5 Net current density versus output voltage for various electron lifetimes for W=0.5 μm and $\tau_p = 2\times10^{-9}$ s.

The power conversion efficiency increases from 8.54% to 9.74 % for enhancing the hole lifetime from 2×10^{-9} s to 2×10^{-8} s (one order of magnitude increase). Electron lifetime mainly affects the open circuit voltage as shown in Fig. 4.5. Grain growth and recrystallization can reduce recombination and thus enhances the carrier lifetime. Razykov *et al,* [62] have developed an efficient deposition technique (chemical molecular beam deposition) to increase the grain size and to ensure high quality CdTe films.

4.5.4 Effects of acceptor concentration

Effect of acceptor concentration on the *J-V* characteristics is shown in Fig. 4.6. The acceptor concentration has a negligible impact on J_{sc} but it greatly affects V_{oc}. Low acceptor concentration reduces the built-in potential of the *pn* junction and enhances the dark current [47]. Thus lower acceptor concentration reduces V_{oc}.

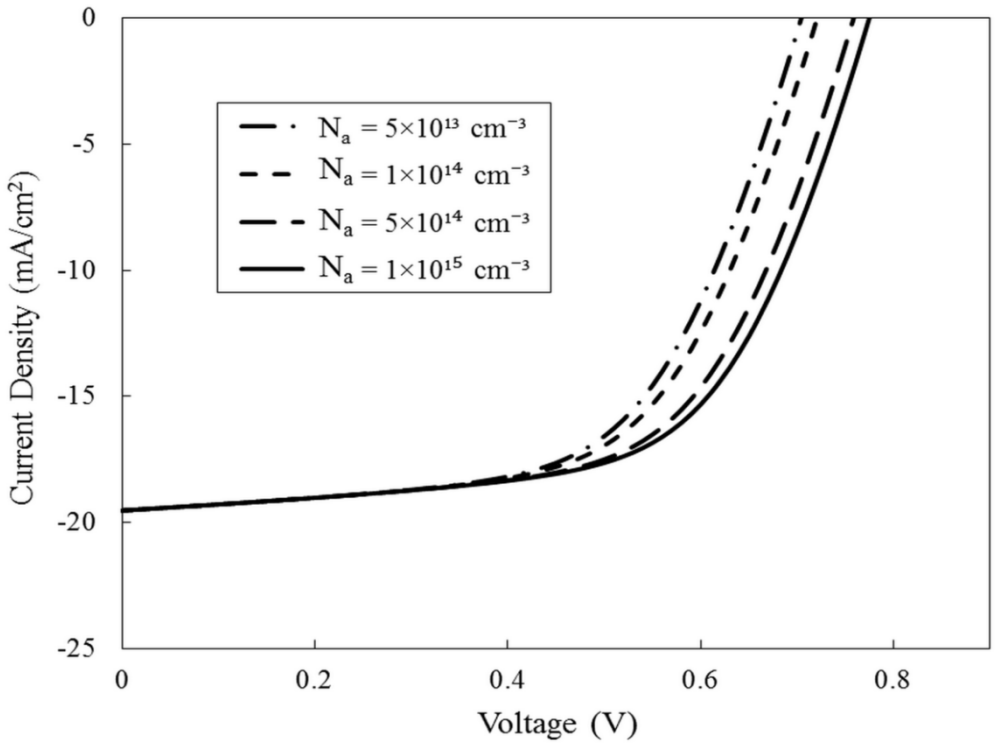

Figure 4.6 Effect of acceptor concentration on the *J-V* characteristics of CdTe/CdS solar cells for $W = 0.5$ μm, $\tau_n = 10^{-10}$ s and $\tau_p = 2\times10^{-9}$ s

4.5.5 Impact of series resistance

As mentioned before, the value of series resistance depends on semiconductor materials, contact resistance (resistance between semiconductor and electrode), the resistance of the electrode materials and deposition technique. The practical devices are more prone to the effects of series resistance whereas an ideal solar cell has the minimum series resistance. Figure 4.7 shows that the increasing value of series resistance reduces the FF of the *J-V* curve. The width of the absorber layer is kept fixed at 0.5 μm and the acceptor concentration is 10^{14} cm^3. The values of other parameters are taken from Table 3.1 and 4.1.

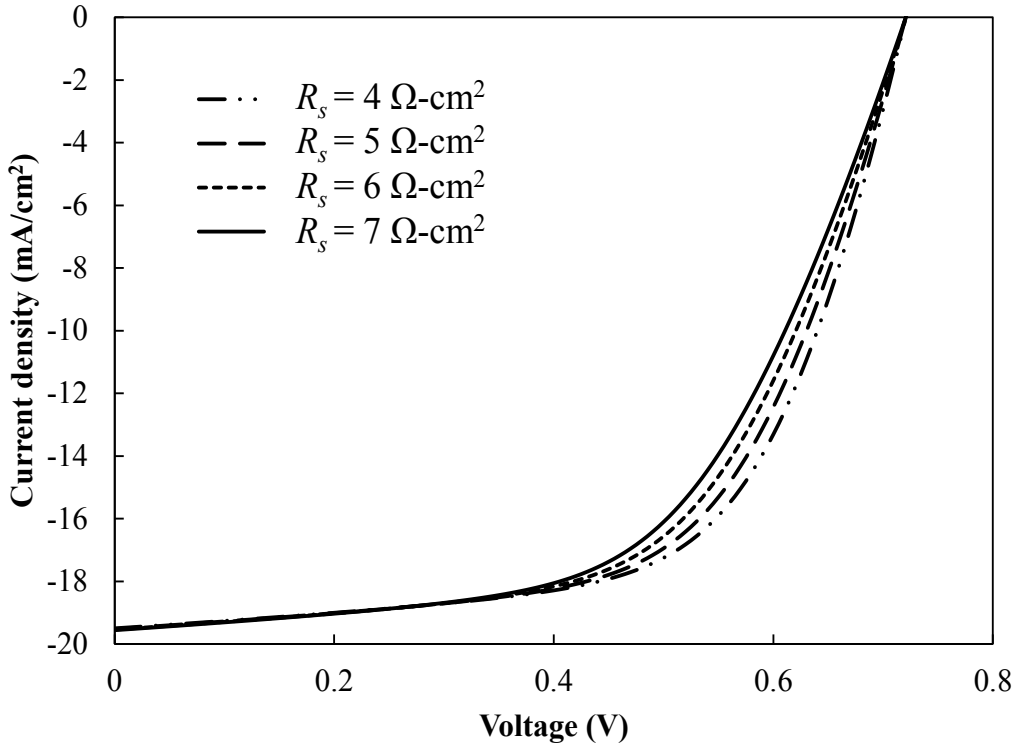

Figure 4.7 Effect of series resistance on *J-V* characteristic

4.6 Summary

An analytical model has been derived considering both drift and diffusion of charge carriers. The model shows good agreement with the published experimental results. It is evident from the simulations, that the hole lifetime decreases due to increased number of defect states in the absorber, while the width of the absorber layer is reduced from 1.1 μm to 0.5 μm. The acceptor concentration does not have any significant effect on the J_{sc}. However, V_{oc} reduces if the acceptor concentration decreases. The effects of carrier lifetime and series resistance have also been illustrated in this chapter. It has been found that the cell performance mainly depends on the hole transport properties. Therefore, the hole lifetime must be improved in order to increase the efficiency of a CdS/CdTe thin-film solar cell.

CHAPTER 5

Analytical Model for Current-Voltage Characteristics of Bulk Heterojunction Organic Solar Cells

5.1 Abstract

An analytical model, incorporating exponential photon absorption, carrier trapping, carrier drift and diffusion in the active layer, is derived to study the current-voltage characteristics of P3HT:PCBM solar cells. The Modified Braun's model is used to compute the electric field dependent dissociation efficiency of the bound electron-hole pairs (EHPs). The overall load current is calculated considering the actual solar spectrum and voltage dependent dark current density. The analytical model is then verified by published experimental results. The effect of dissociation on the current-voltage (*J-V*) characteristics is illustrated. The output of the model suggests that annealing at high temperature increases device performance by improving carrier lifetime and mobility. It is evident from the simulations that bis[70]PCBM, as an acceptor, increases the open circuit voltage (V_{oc}) by reducing the offset between lowest unoccupied molecular orbitals of the acceptor and donor. The effects of carrier lifetime on device performance are also studied. The results of this chapter indicate that the improvement of the charge transport properties (i.e., carrier mobility) in P3HT:PCBM solar cells is extremely important to increase the power conversion efficiency.

5.2 Introduction

Bulk heterojunction (BHJ) polymer solar cells based on blends of conjugated polymers and fullerene derivatives have drawn a lot of attention in research due to their cost effective fabrication process, high conversion efficiency and abundant availability [22]. However, high binding energy of the bound electron-hole pairs (EHPs), due to low dielectric constant (ε_r) of organic materials, reduces the number of photo-generated carriers [24]. Therefore, the photocurrent is dominated by the dissociation efficiency of bound EHPs. Overall cell efficiency also depends on carrier transport properties. A complete understanding of the physics of organic materials and charge transport mechanism can lead this technology one step closer to large scale commercial production. Hence, a physics-based model that relates the quantitative effects of dissociation efficiency and charge transport properties of the materials with the *J-V* characteristic is necessary.

The potential difference between donor (conjugated polymer) and acceptor (soluble fullerene derivative) near the interface helps to dissociate the bound EHPs. Poly(3-hexylthiophene) (P3HT) and [6,6]-phenyl C_{61}-butyric acid methyl ester (PCBM) are used as donor and acceptor, respectively. The weight ratio of P3HT:PCBM in the blend is approximately 1:1. The total length of the active layer (W) is ~100-250nm. The photons are absorbed in the active layer, leading to the creation of excitons. Photo-carrier generation takes place if the bound EHPs successfully diffuse to the dissociation sites. In BHJ polymer solar cells, the electron donor and acceptor are blended together to spread dissociation sites all over the active layer (P3HT:PCBM blend). The resulting free

electrons and holes transport through acceptor and donor component of the blend, respectively.

Few models have been proposed in the literature for calculating voltage-dependent photocurrent in BHJ polymer solar cells [25, 27]. However, the analytical models are based on empirical expressions. The second model does not consider direct recombination of photo-carriers and also fails to explain the dissociation of bound EHPs. Blom *et al.* [25] mentioned an analytical model to explain the *J-V* characteristics of BHJ solar cell. The model uses Braun model, which is based on Onsager theory, to compute the escape probability, even though there is significant difference between Braun model and the exact extension of Onsager theory. Modified Braun's model agrees well with the exact extension of Onsager theory in low field. As solar cells consist of P3HT:PCBM blend operate in low field, using Modified Braun's model is more appropriate for calculating the escape probability [44].

In this chapter, an analytical model for voltage-dependent photocurrent has been derived considering electric field dependent escape probability. The probability of EHPs separation is known as escape probability. Modified Braun model, which shows good agreement with the exact extension of Onsager theory at low electric field, is used to determine the dissociation of the bound EHPs. Exponential photon absorption and actual solar spectrum are considered in the model to compute the photocurrent densities at various output voltages. The incident photon flux is taken as the air mass (AM) 1.5 global spectrum from the ASTM G-173-03 standard [48]. The overall load current is calculated

considering the effects of voltage dependent forward dark current. The analytical model is then compared with the published experimental results in order to determine the carrier transport properties (defects, carrier mobility and lifetime) and effects of charge dissociation.

5.3 Modified Braun Model

As mentioned earlier, most of the *J-V* characteristic models are based on Onsager theory. However, Onsager assumed that geminate recombination takes place at zero reaction radius [44]. Reaction radius is the minimum distance required between bound electron and hole to recombine. This assumption leads to a very low separation rate compared to the observed escape probability in P3HT:PCBM blends. Therefore, it is believed that bound electron and hole recombine at a nonzero distance [43]. Thus Onsager theory fails to explain the exact behavior of the geminate pairs under the influence of a built-in electric field.

Braun proposed an empirical model to compute electric field depended escape probability, assuming geminate recombination occurs at a nonzero reaction radius. The expression for electric field depended dissociation rate proposed by Braun is given as [25].

$$M(F) = \frac{K_d(F)}{K_d(F)+K_f} \tag{5.1}$$

Here, F is the electric field, M is the escape probability, K_d is the separation rate, K_f $(= \frac{S_1}{a})$ is the recombination rate of bound EHPs, a is the reaction radius (or initial

separation of electron and hole), S_1 is the reactivity parameter. Reactivity parameter is the relative velocity between bound electron and hole at the reaction radius. It governs the reactivity of the bound electrons and holes. However, Wojcik *et al.* [44] claim that Eq. 5.1 is not accurate because both recombination and separation processes are assumed to follow exponential kinetics. They showed that Modified Braun model agrees well with the exact extension of Onsager theory except at very high electric field. According to the Modified Braun's model [44],

$$K_d(F) = \frac{Dr_c}{a^3 e^{r_c/a}} J_1\left[2\sqrt{2}(-C_1)^{1/2}\right]/\sqrt{2}\,(-C_1)^{1/2} \tag{5.2}$$

$$M(F) = \left[1 + \frac{K_f a^3 e^{r_c/a}}{Dr_c J_1\left[2\sqrt{2}(-C_1)^{1/2}\right]/\sqrt{2}(-C_1)^{1/2}}\right]^{-1} \tag{5.3}$$

Where D is the sum of the diffusion coefficients of electrons and holes in respective mediums, r_c ($=e^2/4\pi\varepsilon_o\varepsilon_r k_b T$) is the Onsager radius, J_1 is the first order Bessel function, $\varepsilon_o\varepsilon_r$ is the effective dielectric constant of the blend, e is the elementary charge, k_b is the Boltzmann constant, T is the absolute temperature and the reduced field, $C_1 = e^3F/8\pi\varepsilon_o\varepsilon_r k_b^2 T^2$.

5.4 Voltage dependent photocurrent density

An analytical model is derived to calculate the voltage dependent photo current density. The continuity equation is solved to estimate the photo-generated carrier density hence, the total photo-current density. Few assumptions, such as, uniform electric field F in depletion region, negligibly small thermal equilibrium charge carrier concentration,

constant drift mobility (μ) and a single lifetime (τ) of holes and electrons in the donor and acceptor, respectively, are made to allow the problem to be analytically tractable.

5.4.1 Net current density

The net external current density from a solar cell is [54],

$$J(V) = J_d(V) + \frac{V - JR_s}{R_p} - J_{ph}(V) \tag{5.4}$$

where V is the output voltage, J_{ph} is the photocurrent density, R_s is the series resistance, R_p is the shunt resistance and J_d is the forward diode current density.

5.4.2 Dark current density

The expression of J_d can be given as [56,57],

$$J_d(V) = J_o e^{\left[\frac{V - JR_S}{nV_t}\right]} \tag{5.5}$$

Here, J_o is the reverse saturation current density, $V_t \left(= {k_b T}/{e} \right)$ is the thermal velocity and n is the ideality factor.

5.4.3 EHP generation rate

The electron-hole pair generation rate G in the active layer can be written as [21],

$$G(\lambda, V) = \alpha(\lambda)[1 - R(\lambda)]\lambda I_o(\lambda) M/hc \tag{5.6}$$

where I_o is the intensity of the solar spectra (W/cm^2-nm), c is the speed of light, h is the Plank constant, M is the field dependent dissociation efficiency, R loss factors, $\alpha(\lambda)$ is the absorption coefficient of the blend, λ is the incident photon wavelength.

5.4.4 Voltage dependent photocurrent density

The steady-state continuity equation for holes is [29],

$$\frac{\partial}{\partial t}(\delta p) = \mu_p F \frac{\partial}{\partial x}(\delta p) + D_p \frac{\partial^2 \delta p}{\partial x^2} + G e^{-\alpha(\lambda)x} - \frac{\delta p}{\tau_p} = 0 \tag{5.7}$$

where δp is photo generated hole concentration, x is the distance along the active layer from the front contact, D is the diffusion coefficient, α is the absorption coefficient of the blend and G is the EHP generation rate at $x = 0$. Here the subscript p represents holes. Due to the built-in field in the active layer, photo-generated holes immediately start drifting towards the front contact ($i.e., \delta p = 0$ at $x = W$) and recombine near the front contact at a velocity of S_p. Thus the solution of Eq. 5.7 is,

$$\delta_p(x, \lambda) = C_1 e^{m_1 x} + C_2 e^{m_2 x} + A e^{-\alpha x} \tag{5.8}$$

where

$$m_1 = \frac{-\mu_p F + \sqrt{\mu_p^2 F^2 + 4\frac{D_p}{\tau_p}}}{2D_p} \tag{5.9}$$

$$m_2 = \frac{-\mu_p F - \sqrt{\mu_p^2 F^2 + 4\frac{D_p}{\tau_p}}}{2D_p} \tag{5.10}$$

$$A = \frac{G\tau_p}{1+F\mu_p\tau_P\alpha-D_p\tau_p\alpha^2} \tag{5.11}$$

$$C_2 = \frac{A\left[e^{m_1W}(D_p\alpha-S_p)+e^{-\alpha W}(S_p+D_pm_1)\right]}{e^{m_1W}(S_p+D_pm_2)-e^{m_2W}(S_p+D_pm_1)} \tag{5.12}$$

$$C_1 = \frac{-C_2e^{m_2W}-Ae^{-\alpha W}}{e^{m_1W}} \tag{5.13}$$

The photo current density for the holes which are travelling towards the front contact is,

$$J_p(\lambda,V) = \frac{e}{W}\left\{\mu_pF\int_0^W \delta p dx - D_p\int_0^W \frac{\partial\delta p}{\partial x}dx\right\}$$

$$= \frac{e}{w}\left[C_1(e^{m_1W}-1)\left(\frac{\mu_pF}{m_1}-D_p\right)+C_2(e^{m_2W}-1)\left(\frac{\mu_pF}{m_2}-D_p\right)-\right.$$

$$\left.A(e^{-\alpha W}-1)\left(\frac{\mu_pF}{\alpha}+D_p\right)\right] \tag{5.14}$$

Similarly, the photo current density for electrons is,

$$J_n(\lambda,V) = \frac{e}{w}\left[C_1'\left(e^{m_1'W}-1\right)\left(\frac{\mu_nF}{m_1'}+D_n\right)+C_2'\left(e^{m_2'W}-1\right)\left(\frac{\mu_nF}{m_2'}+D_n\right)+\right.$$

$$\left.A'(e^{-\alpha W}-1)\left(D_n-\frac{\mu_nF}{\alpha}\right)\right] \tag{5.15}$$

where

$$m_1' = \frac{\mu_nF+\sqrt{\mu_n^2F^2+4\frac{D_n}{\tau_n}}}{2D_n} \tag{5.16}$$

$$m_2' = \frac{\mu_nF-\sqrt{\mu_n^2F^2+4\frac{D_n}{\tau_n}}}{2D_n} \tag{5.17}$$

$$A' = \frac{G\tau_n}{1-F\mu_n\tau_n\alpha-D_n\tau_n\alpha^2} \tag{5.18}$$

$$C_2' = \frac{A'\left[e^{-\alpha W}(D_n\alpha-S_n)+e^{m_1'W}(S_n+D_nm_1')\right]}{S_n\left(e^{m_2'W}-e^{m_1'W}\right)+D_n\left(m_2'e^{m_2'W}-m_1'e^{m_1'W}\right)} \tag{5.19}$$

$$C_1' = -(A' + C_2') \tag{5.20}$$

The total photo current density can be obtained by integrating over all incident photon wavelengths of the solar spectrum, i.e.,

$$J_{ph}(V) = \int_0^\infty \{J_p(\lambda, V) + J_n(\lambda, V)\} d\lambda \tag{5.21}$$

The external voltage-dependent average electric field in the depletion region is given by [20],

$$F(V) = \frac{V_{bi}-V_j}{W} = \frac{V_{bi}-(V-JR_s)}{W} \tag{5.22}$$

where V_j (=$V - JR_s$) is the junction voltage, R_s is the series resistance and V_{bi} is the built-in potential voltage. The V_{bi} is determined by the deference between the work functions of anode and cathode [63]. Typically, the V_{bi} in a P3HT:PCBM blend is around 0.8 V.

5.5 Results and discussions

5.5.1 Experimental fit at different intensities

The analytical model is verified by fitting with the published experimental data. The absorption coefficients of the blend at different wavelengths have been taken from Fig. 2 of Ref. [35]. Figure 5.1 illustrates the absorption coefficient versus wavelength curve of P3HT:PCBM blend.

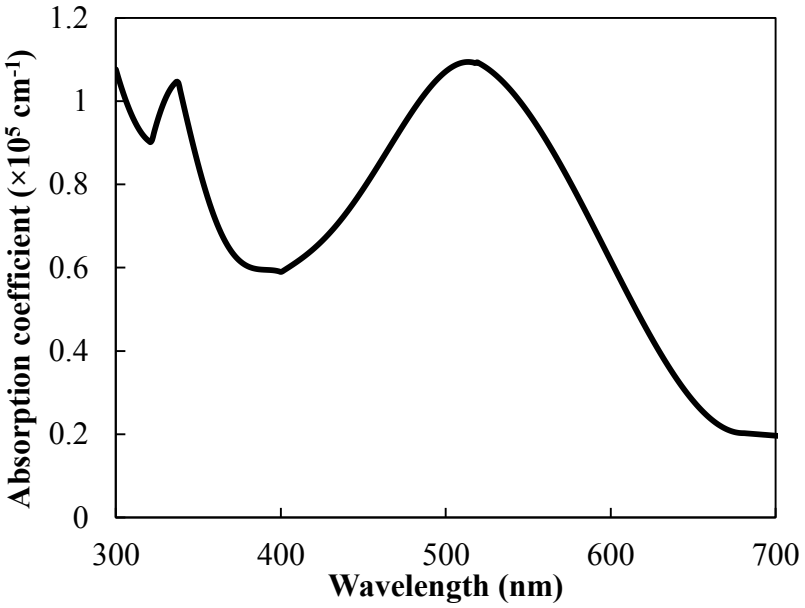

Figure 5.1 Absorption coefficienct of P3HT:PCBM blend [35]

The carrier mobility and lifetime are kept within an acceptable range while the experimental results are reconstructed [22,64]. Figure 5.2 shows the *J-V* curves of P3HT:PCBM solar cells at different sun intensities (i.e., 0.5, 0.75, 1 and 1.4 sun) for *W*=230 nm. The symbols represent experimental data, and the solid lines represent the

analytical results. The experimental data for different sun intensities are extracted from Fig. 4a of Ref. [65].

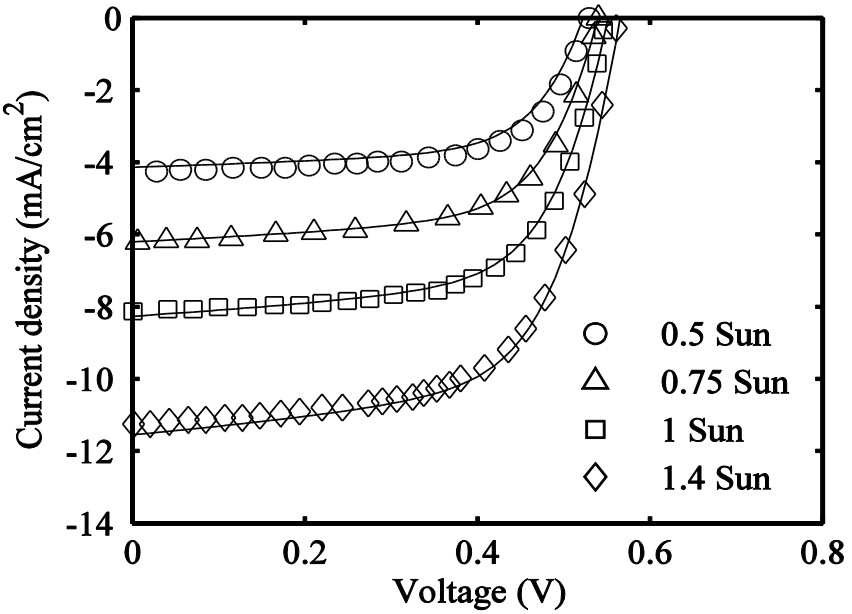

Figure 5.2: *J-V* characteristic at different sun intensities. The symbols represent experimental data and solid lines represent the theoretical fit to the experimental data

The μ_p in P3HT is 2×10^{-4} cm^2/V-s and μ_n in PCBM is 5×10^{-3} cm^2/V-s. The electron (in PCBM) and hole lifetimes (in P3HT) are 6×10^{-5} and 3×10^{-5} s, respectively. The reaction radius (a) of a bound EHP is considered to be ~1.5 nm, the reactivity parameter (S_1) is kept fixed at 0.05 cm/s and the dielectric constant (ε_r) of P3HT:PCBM blend is 3.5 [25, 24]. Since the analytical model agrees well with the experimental results, we use the analytical model to examine the effects of dissociation efficiency and carrier lifetimes on the *J-V* characteristics.

5.5.2 Effects of dissociation

Dissociation of bound EHPs has great impact on cell efficiency. The effect of dissociation on *J-V* curve is shown in Fig. 5.3. The values of the parameters used to reproduce the experimental data (Fig. 5.2) are also used here to observe the effect of dissociation. The solid line represents the *J-V* characteristic of P3HT:PCBM solar cell with regular dissociation rate, dotted-dashed line represents *J-V* curve assuming complete charge collection and the dashed line represents *J-V* characteristic considering complete dissociation of bound EHPs. The cell efficiency increases by only 0.15% (from 2.87% to 3.02%) when complete charge collection is assumed. On the other hand, cell efficiency increases from 2.87% to 3.74% when complete dissociation of bound EHP is assumed. The difference between overall efficiencies implies that dissociation of bound EHPs is the dominating factor on the efficiency of BHJ polymer solar cells.

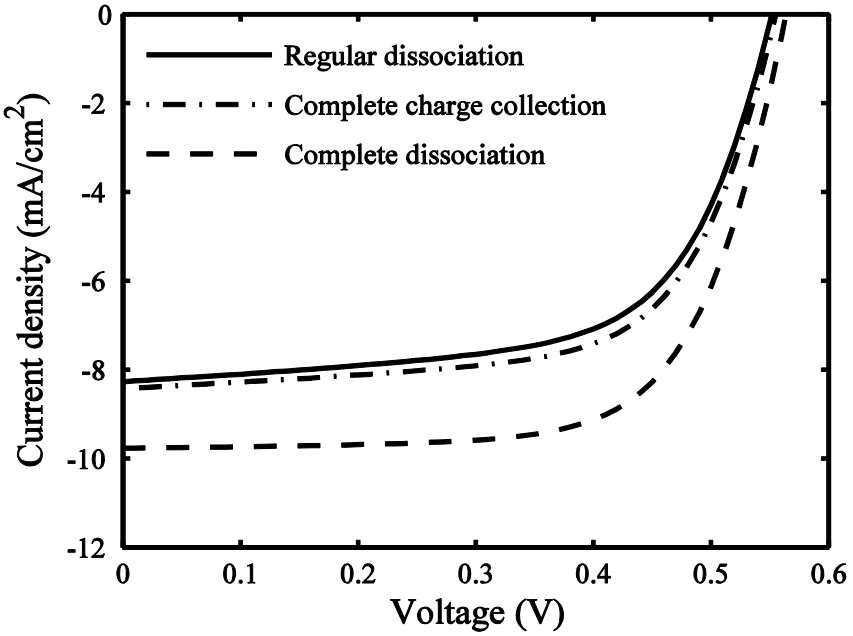

Figure 5.3 Net current density versus voltage curves of P3HT:PCBM solar cells assuming complete charge collection (dotted-dashed line) and complete dissociation of bound EHPs (dashed line). The solid line represents *J-V* characteristic with regular dissociation of bound EHPs

5.5.3 Effects of carrier lifetimes

As the holes are slower compared to electrons inside the active layer, the efficiency of P3HT:PCBM solar cells is more prone to hole lifetime than to electron lifetime. The overall theoretical efficiency of the cell decreases from 3% to 1.7% when the hole lifetime is changed from 3×10^{-4}s to 3×10^{-7}s but for approximately same variation of electron lifetime, the efficiency decreases from 2.8% to 2.3%. The effects of τ_n and τ_p for the W = 230 nm are shown in Figs. 5.4 and 5.5, respectively. The addition of alkyl thiol molecules to the blend increases the structural order and thus improves carrier lifetime [66]. The power conversion efficiency increases from 2.87% to 3% for enhancing the hole lifetime from 3×10^{-5} s to 3×10^{-4} s (one order of magnitude increase).

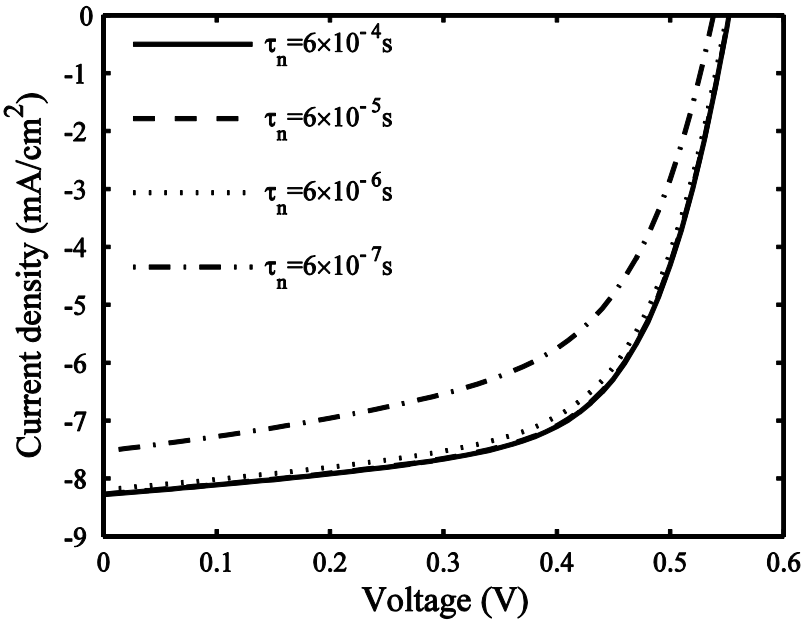

Figure 5.4 Net current density versus output voltage for various electron lifetimes (τ_p = 3×10^{-5} s)

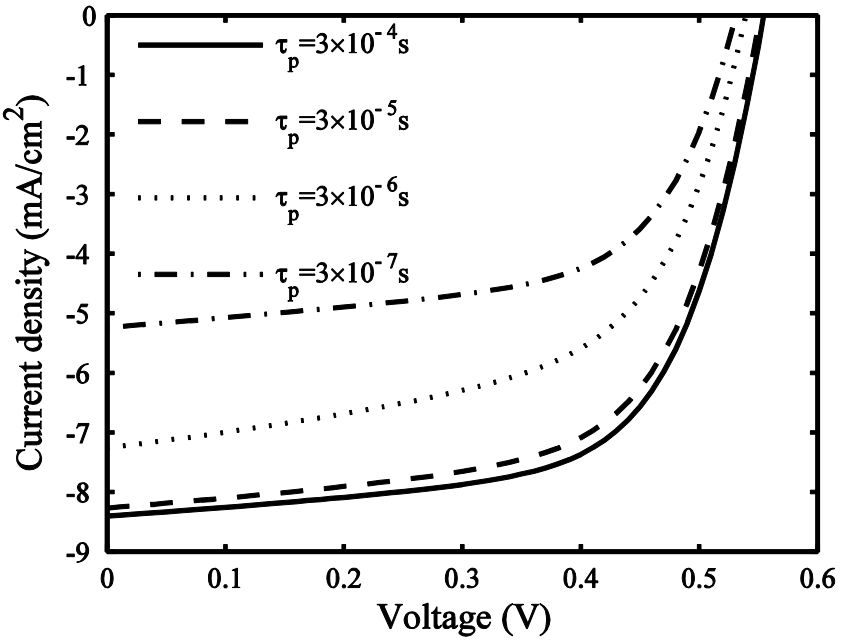

Figure 5.5 Net current density vs. output voltage for various hole lifetimes (τ_n = 6×10^{-5} s)

5.5.4 Annealed vs. as-cast solar cells

The *J-V* curves of as-cast solar cell, annealed (at 75°C for 4 minutes) solar cell and cell simultaneously treated by annealing under an external electric field are shown in Fig. 5.6. The experimental values are extracted from Ref. [67]. The width of the active layer is kept fixed at 120 nm.

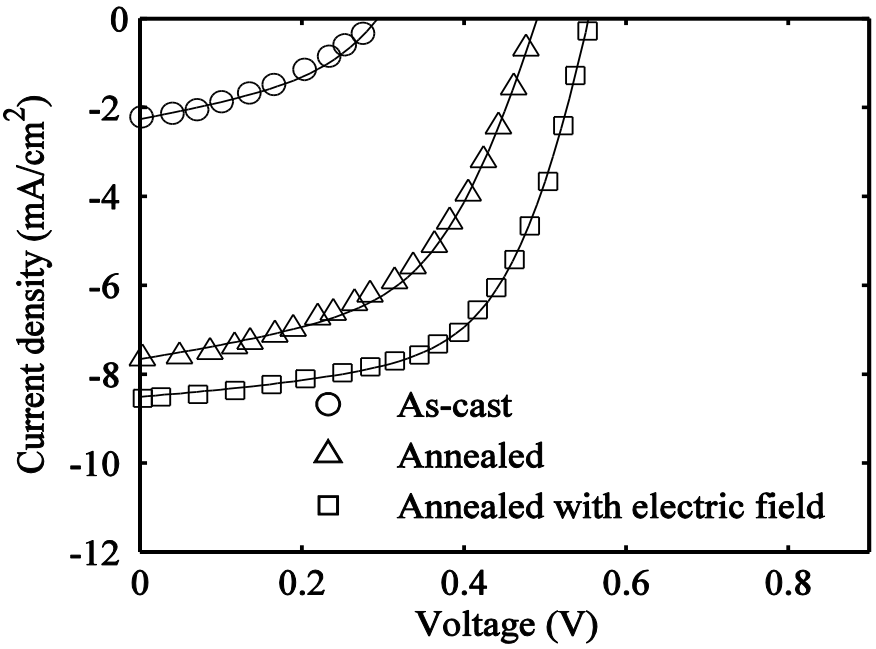

Figure 5.6 *J-V* curves of P3HT:PCBM solar cells: as cast solar cell (circles), annealed solar cell (triangles) and cells simultaneously treated by annealing and applying an external electric field (squares). The solid lines represent the theoretical fit to the experimental data

The absorption coefficient of the blend improves due to annealing [35]. Different set of absorption coefficients (Ref. [38]) is used to compute the *J-V* curve of as-cast solar cell. The absorption coefficients of different wavelengths of non-annealed P3HT:PCBM blend is illustrated in Fig. 5.7.

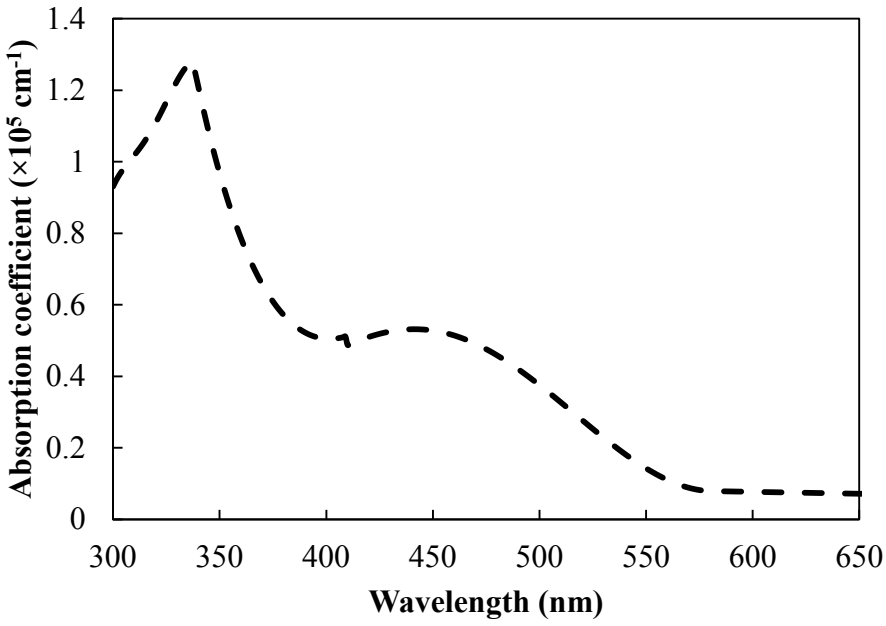

Figure 5.7 Absorption coefficienct of as-cast P3HT:PCBM blend [38]

High absorption increases the photo-generation and, hence, affects the short circuit current density (J_{sc}). It is evident from the simulations that low mobility of charge carriers in the blend is one of the main factors limiting the performance of BHJ solar cells. It is because low mobility hinders the excitons to travel to the donor acceptor interface and also affects carrier transportation after dissociation. Due to increased crystallization, near one order magnitude enhancement of hole mobility of the polymer is observed in annealed solar cells. The reactivity parameter also increases with carrier mobility in annealed solar cells. Presence of an external field during annealing leads to further improvement of charge carrier mobility due to an orientation of the polymer chains in the direction of the applied field. Annealing at a high temperature also burns the shunt paths [68]. As a result, shunt resistance increases by a large number (~10^3) in

annealed solar cells. The carrier lifetime, carrier mobility, reactivity parameter and shunt resistance of P3HT:PCBM solar cells treated by different annealing processes (i.e., annealing with and without external electric field) and as-cast solar cell are given in Table 5.1.

Table 5.1 Carrier lifetime, carrier mobility, reactivity parameter and shunt resistance of as-cast and differently treated P3HT:PCBM solar cells

Parameters	As-cast	Annealed	Annealed in presence of electric field
Hole lifetime, τ_p (s)	6×10^{-6}	8×10^{-5}	9×10^{-5}
Electron lifetime, τ_n (s)	1×10^{-5}	4×10^{-5}	6×10^{-5}
Hole mobility, μ_p (cm^2/V-s)	5×10^{-5}	1×10^{-4}	2×10^{-4}
Electron mobility, μ_n (cm^2/V-s)	3.5×10^{-4}	1×10^{-3}	3×10^{-3}
Reactivity parameter, S_1 (cm/s)	6×10^{-3}	1×10^{-2}	1×10^{-2}
Shunt resistance, R_{sh} (Ω-cm^2)	9.9×10^{2}	7.8×10^{5}	1×10^{6}

5.5.5 bis[70]PCBM as an acceptor

Another promising way to increase the efficiency of P3HT:PCBM solar cells is tuning the L UMO-A, with respect to the LUMO of the donor, LUMO-D [36]. Usually the energy difference between LUMO-A and LUMO-D is 1.1 eV. Whereas, only 0.4 eV offset between LUMO-A and LUMO-D is sufficient for successful dissociation of the bound EHPs in P3HT:PCBM blend [25]. As a result, this excess energy of the carriers is dissipated. Thus the open circuit voltage (V_{oc}), which is restricted by the difference between LUMO-A and HOMO of the donor, HOMO-D, is greatly affected. Lenes *et al.* [36] introduce bisadduct analogues of C_{70} as acceptor to decrease the offset (by increasing the LUMO-A) between LUMO-A and LUMO-D. Figure 5.8 shows the *J-V*

characteristics of P3HT:PCBM and P3HT:bis[70]PCBM solar cells for W=200nm. The reverse saturation current density, reactivity parameter and carrier mobility are given in Table 5.2. Decrease in electron mobility hints towards the presence of shallow trap centers. Thus the reduction of J_{sc} can be explained through an increase in irregularity in the PCBM. Replacing the PCBM layer with bis[70]PCBM also effects the energy difference between LUMO-A and HOMO-D, which is reflected in the reverse saturation current densities of P3HT:PCBM and P3HT: bis[70]PCBM solar cells.

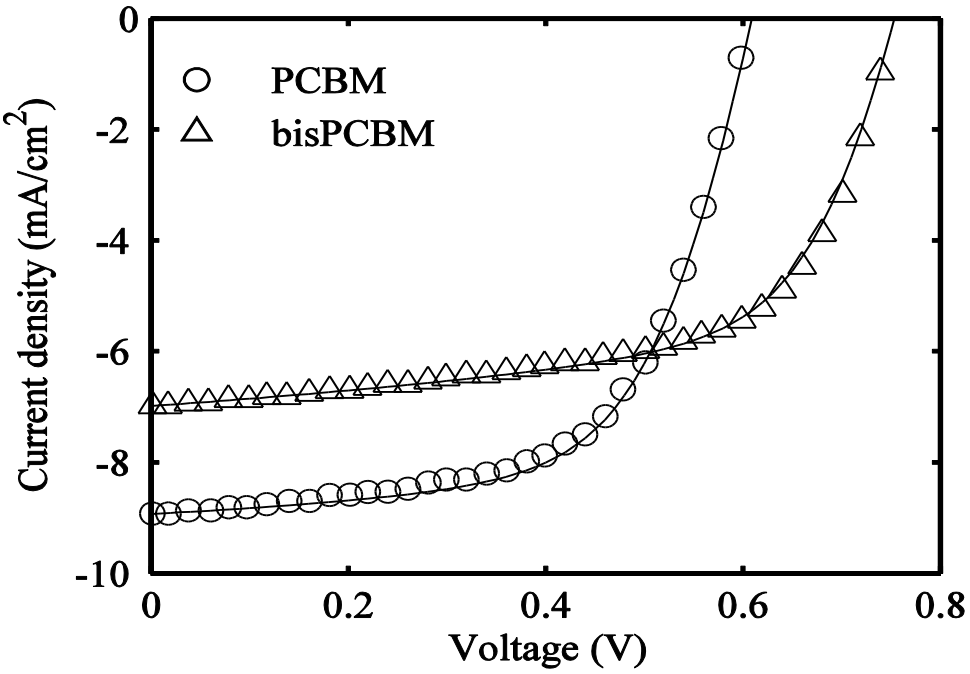

Figure 5.8 *J-V* characteristics of P3HT:PCBM and P3HT:bis[70]PCBM solar cells. The symbols represent the experimental values and the solid lines represent the theoretical fit to the experimental data

Table 5.2. Carrier mobility, reactivity parameter and reverse saturation current density of P3HT:PCBM and P3HT:bis[70]PCBM solar cells.

Parameters	PCBM	bisPCBM
Electron mobility, μ_n (cm^2/V-s)	1.5×10^{-3}	6×10^{-4}
Hole mobility, μ_p (cm^2/V-s)	1×10^{-4}	1×10^{-4}
Reverse saturation current density, J_o (A/cm^2)	2.7×10^{-8}	1×10^{-9}
Reactivity parameter, S_1 (cm/s)	1.5×10^{-2}	1×10^{-2}

5.6 Summery

An analytical model for voltage dependent current density in BHJ solar cell has been developed. The model considers both diffusion and internal field assisted drift of the charge carriers in the active region. The model agrees well with the experimental results. It has been shown that cell performance is more prone to dissociation of bound EHPs rather than to charge collection efficiency. The effects of carrier lifetimes on *J-V* curves have also been illustrated in the chapter. It is apparent from the results that the hole lifetime increases by one order of magnitude, due to increased crystallization, while the blend is annealed at high temperature. Annealing also burns the shunt paths. Replacing PCBM with bis[70]PCBM, increases V_{oc} by reducing the offset between LUMOs and reduces J_{sc}.

CHAPTER 6

Conclusions, Contributions and Future Work

6.1 Conclusions

It is found that the drop in cell performance with decreasing absorber thickness is due to both incomplete absorption and charge collection. The CdS/CdTe solar cell efficiency depends critically on the transport properties of the holes. A good agreement of the analytical and numerical models with experimental data is ensured by reducing carrier lifetime in the thinner absorber layers. It suggests an increase in defect density and recombination states for holes in thinner absorbers. The results of this paper indicate that the improvement of the charge transport properties in submicron CdTe solar cells is extremely important to improve the power conversion efficiency.

The Modified Braun's model, which shows good agreement with exact extension of Onsager theory at low field, is used to calculate dissociation efficiency of the bound EHPs in P3HT:PCBM organic solar cell. We have found that complete dissociation of EHPs improves the cell performance much more than complete charge collection does. Carrier lifetime also has great impact on cell efficiency. The effects of electron and hole lifetime on *J-V* characteristics are shown. It is evident that the cell performance is more sensitive to hole lifetime than to electron lifetime. An increment of hole lifetime by one order of magnitude can improve the cell efficiency by more than 1%. It has been noticed

that the presence of shunt paths is reduced in annealed solar cells. Annealing increases the regularity of P3HT and as a consequence, the hole mobility is also improved. Thus, annealing increases the overall efficiency of solar cells based on P3HT:PCBM blend. Annealing in presence of an external electric field leads to further improvement in cell performance. The reverse saturation current density (J_o) reduces when bis[70]PCBM is used as an acceptor. This reduction of J_o suggests an increase of energy difference between LUMO-A and HOMO-D. At the same time the offset between LUMOs of donor and acceptor is reduced. Thus the V_{oc} improves in P3HT: bis[70]PCBM solar cells.

6.2 Contributions

An analytical model to study the current–voltage characteristics of CdS/CdTe thin film solar cells has been developed by considering carrier drift and diffusion in the CdTe layer. The analytical model is verified by Taurus Medici simulation and published experimental results for different absorber layer thicknesses. This work (chapter 4) has been published in journal [53] and conference papers.

- Salman M. Arnab and M. Z. Kabir, "Modeling of the effects of charge transport on voltage-dependent photocurrent in ultrathin CdTe solar cells," *J. Vac. Sci. Technol. A*, vol. 31, pp. 061201, 2013.
- S. M. Arnab and M. Z. Kabir, "Modeling of the Effects of Charge Transport on Voltage-Dependent Photocurrent in Ultra-Thin CdTe Solar Cells" *Photovoltaic Technology Conference 2013,* Aix-en-Provence, France, May 22-24, 2013.

An analytical model has also been derived to investigate the *J-V* characteristics of P3HT:PCBM solar cells. Modified Braun Model has been used to calculate the field depended dissociation of bound EHPs. The work on BHJ organic solar (chapter 5) has been presented is a conference. The proceedings of this conference paper will be considered for publication in *Canadian Journal of physics*.

- S. M. Arnab and M. Z. Kabir, "Modeling of current-voltage characteristics of bulk heterojunction organic solar cells," *25th International Conference on Amorphous and Nano-crystalline Semiconductors,* Toronto, Canada, August 18-23, 2013.
- "Modeling of current-voltage characteristics of bulk heterojunction organic solar cells," will later be submitted to *Canadian Journal of Physics*. -under preparation.

6.2 Future work

The efficiency of thin-film solar cells can be increased by adding an extra layer for down-conversion. The analytical model for CdS/CdTe thin-film solar cells can be extended further more to incorporate the effects of down-conversion. This model can also be verified with $Cu(InGa)Se_2$ thin-film solar cells. The models developed for both thin-film and BHJ solar cells, do not consider the effects of temperature on various parameters (i.e., carrier mobility). Therefore, temperature effects can be included in both the models.

References

[1] C. Grätzel and S. M. Zakeeruddin, “Recent trends in mesoscopic solar cells based on molecular and nanopigment light harvesters,” *Materialstoday*, vol. 16, pp. 11, 2013.

[2] Energy Information Administration, Annual Energy Outlook 2013, source: http://www.eia.gov/forecasts/aeo/er/pdf/appa.pdf.

[3] L. Zhu, J. K. Luo, G. Shao, and W.I. Milne, “On optical reflection at heterojunction interface of thin film solar cells,” *Solar Energy Materials & Solar Cells*, vol. 111, pp. 141, 2013.

[4] G. A. Meehl, T. F. Stocker, W. D. Collins, P. Friedlingstein, A. T. Gaye, J. M. Gregory, A. Kitoh, R. Knutti, J. M. Murphy, A. Noda, S. C. B. Raper, I. G. Watterson, A. J. Weaver, and Z. -C. Zhao, Global Climate Projections. In: Climate Change 2007: The Physical Science Basis. Contribution of Working Group I to the Fourth Assessment Report of the Intergovernmental Panel on Climate Change, Cambridge University Press, Cambridge, United Kingdom and New York, NY, USA, 2007.

[5] Ohl RS. "Light sensitive device" U.S. Patent 2,402,662 Issue date: June 1946.

[6] H. Spanggaard, and F. C. Krebs, “A brief history of the development of organic and polymeric photovoltaics,” *Solar Energy Materials & Solar Cells*, vol. 83, pp. 125, 2004.

[7] L. Dou, J. You, J. Yang, C. -C. Chen, Y. He, S. Murase, T. Moriarty, K. Emery, G. Li, and Y. Yang, “Tandem polymer solar cells featuring a spectrally matched low-bandgap polymer,” *Nature Photonics*, vol. 6, pp. 180, 2012.

[8] M. A. Green, Third Generation Photovoltaics: Advanced Solar Energy Conversion, (Springer, New York, 2003).

[9] Solarbuzz, Annual PV Market Report, source: http://solarcellcentral.com/markets_page.html on July, 2013.

[10] P. Heremans, D. Cheyns, and B. P. Rand, "Strategies for increasing the efficiency of heterojunction organic solar cells: material selection and device architecture," *Accounts of Chemical Research*, vol. 42, pp. 1740, 2009.

[11] Y. Liang, Z. Xu, J. Xia, S. –T. Tsai, Y. Wu, G. Li, C. Ray, and L. Yu, "For the Bright Future—Bulk Heterojunction Polymer Solar Cells with Power Conversion Efficiency of 7.4%," *Advanced Materials*, vol. 22, pp. E135, 2010.

[12] M. Pagliaro, G. Palmisano, and R. Criminna, Flexible Solar Cells, (Wiley-Vch, Wiley-VCH, Weinheim, 2008).

[13] J. Quiggin, "The End of the Nuclear Renaissance," The National Interest, January 3, 2012, source: http://nationalinterest.org/commentary/the-end-the-nuclear-renaissance-6325.

[14] C. A. Wolden, J. Kurtin, J. B. Baxter, I. Repins, S. E. Shaheen, J. T. Torvik, A. A. Rockett, V. M. Fthenakis, and E. S. Aydil, "Photovoltaic manufacturing: Present status, future prospects, and research needs," *J. Vac. Sci. Technol. A*, vol. 29, pp. 030801, 2011.

[15] A. Goetzberger and V. U. Hoffmann, Photovoltaic Solar Energy Generation, (Springer-Verlag, Berlin Heidelberg, 2005).

[16] P. R. Chalker, P. A. Marshall, S. Romani, J. W. Roberts, S. J. C. Irvine, D. A. Lamb, A. J. Clayton, and P. A. Williams, "Atomic layer deposition of Ga-doped ZnO transparent conducting oxide substrates for CdTe-based photovoltaics," *J. Vac. Sci. Technol. A,* vol. 31, pp. 01A120, 2013.

[17] Z. Bai, J. Yang, and D. Wang, "Thin film CdTe solar cells with an absorber layer thickness in micro- and sub-micrometer scale," *Appl. Phys. Lett.*, vol. 99, pp.143502, 2011.

[18] N. R. Paudel, K. A.Wieland, and A. D. Compaan, "Ultrathin CdS/CdTe solar cells by sputtering," *Solar Energy Materials & Solar Cells*, vol. 105, pp. 109, 2012.

[19] N. Amin, K. Sopian, and M. Konagai, "Numerical modeling of CdS/CdTe and CdS/CdTe/ZnTe solar cells as a function of CdTe thickness," *Solar Energy Materials & Solar Cells*, vol. 91, pp. 1202, 2007.

[20] S. Hegedus, D. Desai, and C. Thompson, "Voltage dependent photocurrent collection in CdTe/CdS solar cells," *Prog. Photovolt: Res. Appl.*, vol. 15, pp. 587, 2007.

[21] M. S. Anjan and M. Z. Kabir, "Modeling of current–voltage characteristics of CdS/CdTe solar cells," *Phys. Stat. Solidi A*, vol. 208, pp. 1813, 2011.

[22] R. C. I. MacKenzie, T. Kirchartz, G. F. A. Dibb, and J. Nelson, "Modeling Nongeminate Recombination in P3HT:PCBM Solar Cells," *J. Phys. Chem. C*, vol. 115, pp. 9806, 2011.

[23] Y. Li and Y. Zou, "Conjugated Polymer Photovoltaic Materials with Broad Absorption Band and High Charge Carrier Mobility," *Advanced Materials*, vol. 20, pp. 2952, 2008.

[24] V. D. Mihailetchi, L. J. A. Koster, J. C. Hummelen, and P.W.M. Blom, "Photocurrent Generation in Polymer-Fullerene Bulk Heterojunctions," *Phys. Rev. Lett.*, vol. 93, pp. 216601, 2004.

[25] P. W. M. Blom, V. D. Mihailetchi, L. J. A. Koster, and D. E. Markov, "Device Physics of Polymer:Fullerene Bulk Heterojunction Solar Cells," *Adv. Mater.,* vol. 19, pp. 1551, 2007.

[26] R. Sokel and R. C. Hughes, "Numerical analysis of transient photoconductivity in insulators ," *J. Appl. Phys.,* vol. 53, pp. 7414, 1982.

[27] P. Schilinsky, C. Waldauf, J. Hauch, and C. J. Brabec, “Citation Simulation of light intensity dependent current characteristics of polymer solar cells,” *J. Appl. Phys.*, vol. 95, pp. 2816, 2004.

[28] J. Nelson, “Polymer:fullerene bulk heterojunction solar cells,” *Materialstoday*, vol.14, pp. 462, 2011.

[29] D. A. Neamen, Semiconductor Physics and Devices: basic principles, (McGraw-Hill, New York, 2003).

[30] J. Poortmans and V. Arkhipov (eds.), Thin film Solar Cells: Fabrication, Characterization and applications, Chapter 7, (Wiley & Sons, England, 2006).

[31] R. Frerichs, “The Photo-Conductivity of "Incomplete Phosphors"”, *Phys. Rev.*, vol. 72, pp. 594, 1947.

[32] R. O. Bell, “Review of optical applications of CdTe,” *Rev. Phys. Appl.* (Paris), vol. 12, pp. 391, 1977.

[33] Z. Bai, J. Yang, D. Wang, “Thin Film CdTe Solar Cells with an Absorber Layer Thickness in Micro- and Sub-Micrometer Scale,” *Appl. Phys. Lett.,* vol. 99, pp. 143502, 2011.

[34] J. C. Nolasco, R. Cabré, J. Ferré-Borrull, L. F. Marsal, M. Estrada, and J. Pallarès, “Extraction of poly (3-hexylthiophene) (P3HT) properties from dark current voltage characteristics in a P3HT/*n*-crystalline-silicon solar cell,” *J. Appl. Phys*., vol. 107, pp. 044505, 2010.

[35] Y. Kim, S. A. Choulis, J. Nelson, and D. D. C. Bradley, “Composition and annealing effects in polythiophene/fullerene solar cells,” *J Mater Sci*, vol. 40, pp. 1371, 2005.

[36] M. Lenes, S. W. Shelton, A. B. Sieval, D. F. Kronholm, J. C. (Kees) Hummelen, and P. W. M. Blom, "Electron Trapping in Higher Adduct Fullerene-Based Solar Cells," *Adv. Funct. Mater.*, vol. 19, pp. 3002, 2009.

[37] S. H Yoo, J. M Kum, and S. O Cho, "Tuning the electronic band structure of PCBM by electron irradiation," *Nanoscale Research Letters,* vol. 6, pp. 545, 2011.

[38] U. Zhokhavets, T. Erb, G. Gobsch, M. A.-Ibrahim, and O. Ambacher, "Relation between absorption and crystallinity of poly(3-hexylthiophene)/fullerene films for plastic solar cells," *Chemical Physics Letters*, vol. 418, pp. 347, 2006.

[39] Y. –H. Lin, Y. –T. Tsai, C. –C. Wua, C. –H. Tsai, C. –H. Chiang, H. –F. Hsu, J. –J. Lee, and C. –Y. Cheng, "Comparative study of spectral and morphological properties of blends of P3HT with PCBM and ICBA," *Organic Electronics*, vol. 13, pp. 2333, 2012.

[40] R Sudharsanan and A Rohatgi,"Growth and process optimization of CdTe and CdZnTe polycrystalline films for high efficiency solar cells," *Solar Cells*, vol. 31, pp. 243,1991.

[41] M Eron and A Rothwarf, "Effects of a voltage-dependent light-generated current on solar cell measurements: CuInSe2/Cd(Zn)S," *Applied Physics Letters*, vol. 44, pp. 131, 1984.

[42] S.Hegedus, "Current-voltage analysis of a-Si and a-SiGe solar cells including voltage-dependent photocurrent collection," *Progress in Photovoltaics*, vol.5, pp. 151, 1997.

[43] C. Deibel, V. Dyakonov, and C. J. Brabec, "Organic Bulk-Heterojunction Solar Cells," *IEEE Journal of Selected Topics in Quantum Electronics*, vol. 16, pp. 1517, 2010.

[44] M. Wojcik and M. Tachiya, "Accuracies of the empirical theories of the escape probability based on Eigen model and Braun model compared with the exact extension of Onsager theory," *J. Chem. Phys.*, vol. 130, pp. 104107, 2009.

[45] P. Schilinsky, C. Waldauf, J. Hauch, and C. J. Brabec, "Citation Simulation of light intensity dependent current characteristics of polymer solar cells," *J. Appl. Phys.*, vol. 95, pp. 2816, 2004.

[46] Medici manual, Synopsis Inc., Mountain View, CA.

[47] S. S. Hegedus and W. N. Shafarman, "Thin-film solar cells: device measurements and analysis," *Prog. Photovolt: Res. Appl.*, vol. 12, pp. 155, 2004.

[48] NREL (http://rredc.nrel.gov/solar/spectra/am1.5/), January, 2013.

[49] S. O. Kasap, Optoelectronics and Photonics: Principles and practices, (Prentice-Hall, Inc., New Jersey, 2001).

[50] J. Fritsche, T. Schulmeyer, D. Kraft, A. Thißen, A. Klein, and W. Jaegermann, "Utilization of sputter depth profiling for the determination of band alignment at polycrystalline CdTe/CdS heterointerfaces," *Appl. Phys. Lett.*, vol. 81, pp. 2297, 2002.

[51] C.S. Ferekides, D. Marinskiy, V. Viswanathan, B. Tetali, V. Palekis, P. Selvaraj, and D.L. Morel, "High efficiency CSS CdTe solar cells," *Thin Solid Films*, vol. 361, pp. 520, 2000.

[52] G. Kartopu, A. J. Clayton, W. S.M. Brooks, S. D. Hodgson, V. Barrioz, A. Maertens, D. A. Lamb, and S. J.C. Irvine, "Effect of window layer composition in $Cd_{1-x}Zn_xS$/CdTe solar cells," *Prog. Photovolt: Res. Appl.,* 2012.

[53] **S. M. Arnab** and M. Z. Kabir, "Modeling of the effects of charge transport on voltage-dependent photocurrent in ultrathin CdTe solar cells," *J. Vac. Sci. Technol. A*, vol. 31, pp. 061201, 2013.

[54] J. Nelson, The Physics of Solar Cells, (Imperial College Press, London, 2003).

[55] C.-T. Sah, R. N. Noyce, and W. Shockley, *Proc. Inst. Radio Electron. Eng.,* vol. 45, pp. 1228, 1957.

[56] S. M. Sze, Semiconductor devices: physics and technology, 2nd ed. (John Wiley & Sons, USA, 2002).

[57] C. S. Solanki, Solar Photovoltaics: fundamentals, technologies and applications, 2nd ed., (PHI Learning Pvt. Ltd., New Delhi, 2011).

[58] A. E. Iverson and D. L. smith, "Mathematical modeling of photoconductor transient response," *IEEE Trans. Electron Devices,* ED-34, pp. 2098, 1987.

[59] M. Miyake, K. Murase, T. Hirato, and Y. Awakura, "Hall effect measurements on CdTe layers electrodeposited from acidic aqueous electrolyte," *J. Electroanal. Chem.,* vol. 562, pp. 247, 2004.

[60] W. K. Metzger, D. Albin, D. Levi, P. Sheldon, X. Li, B. M. Keyes, and R. K. Ahrenkiel, "Time-resolved photoluminescence studies of CdTe solar cells," *J. Appl. Phys.*, vol. 94, pp. 3549, 2003.

[61] V. Plotnikov, X. Liu, N. Paudel, D. Kwon, K.A. Wieland, and A. D. Compaan, "Thin-film CdTe cells: Reducing the CdTe", *Thin Solid Films*, vol. 519, pp. 7134, 2011.

[62] T. M. Razykov, N. Amin, M. A. Alghoul, B. Ergashev, C. S. Ferekides, Y. Goswami, M. K. Hakkulov, K. M. Kouchkarov, K. Sopian, M. Y. Sulaiman, and H. S. Ullal, "Effect of the composition on physical properties of CdTe absorber layer fabricated by chemical molecular beam deposition for use in thin film solar cells," *J. Appl. Phys*., vol. 112, pp. 023517, 2012.

[63] J. Lee, J. Kong, H. Kim, S.-O. Kang, and K. Lee, "Direct observation of internal potential distributions in a bulk heterojunction solar cell," *Appl. Phys. Lett.,* vol. 99, pp. 243301, 2011.

[64] L. J. A. Koster, V. D. Mihailetchi, and P. W. M. Blom, "Ultimate efficiency of polymer/fullerene bulk heterojunction solar cells," *Appl. Phys. Lett.*, vol. 88, pp. 093511, 2006.

[65] C. G. Shuttle, R. Hamilton, B. C. O'Regan, J. Nelson, and J. R. Durrant, "Charge-density-based analysis of the current–voltage response of polythiophene/fullerene photovoltaic devices," *PNAS*, vol. 107, pp. 16448, 2010.

[66] J. Peet, C. Soci, R. C. Coffin, T. Q. Nguyen, A. Mikhailovsky, D. Moses, and G. C. Bazan, "Method for increasing the photoconductive response in conjugated polymer/fullerene composites," *Appl. Phys. Lett.*, vol. 89, pp. 252105, 2006.

[67] F. Padinger, R. S. Rittberger, and N. S. Sariciftci, "Effects of postproduction treatment on plastic solar cells," *Adv. Funct. Mater.*, vol. 13, pp. 85, 2003.

[68] H-J Lee , H-P Kim, H-M Kim, J-H Youn, D-H Nam, Y-G Lee, J-G Lee, A. R. B. M. Yusoff, and J. Jang, "Solution processed encapsulation for organic photovoltaics," *Solar Energy Materials & Solar Cells*, vol. 111, pp. 97, 2013.